catalysts

MDPI

Article

Selective Degradation of Tetracycline by an Adsorption-Coupled Fe-MOF/H_2O_2 Heterogeneous Fenton-like System

Peiguo Zhou *, Jinzhao Hu, Jiaxin Hou and Jiheng Liu

College of Biology and the Environment, Nanjing Forestry University, Nanjing 210037, China; 19819180911@njfu.edu.cn (J.H.); houjiaxin990117@163.com (J.H.); liujiheng@njfu.edu.cn (J.L.)
* Correspondence: zhoupeiguo@njfu.edu.cn

Abstract

Selective degradation of antibiotics in complex wastewater is often hindered by the non-selective consumption of reactive oxygen species by coexisting organic matter. In this study, an adsorption-coupled heterogeneous Fenton-like strategy was developed to preferentially enrich tetracycline (TC) at the catalyst interface prior to oxidative degradation. MIL-53(Fe), MIL-101(Fe), and NH_2-MIL-101(Fe) were synthesized using a solvothermal method and systematically compared in terms of TC adsorption, catalytic degradation, and degradation selectivity in binary TC/glucose systems. Although MIL-101(Fe) exhibited the highest overall TC degradation efficiency, NH_2-MIL-101(Fe) showed the highest selectivity toward TC. At a TC/glucose concentration ratio of 2:2, NH_2-MIL-101(Fe) achieved a TC degradation selectivity of 73.1%, compared with 50.2% for MIL-101(Fe). Electron spin resonance and radical scavenging experiments demonstrated that ·OH was the dominant reactive species and that TC oxidation occurred predominantly at or near the catalyst surface. The enhanced selectivity was attributed to preferential TC adsorption followed by surface-localized oxidation and repeated adsorption–degradation cycles. Full-scan LC-MS analysis revealed several transformation-related ions, from which a tentative pathway involving possible N-demethylation, oxidative fragmentation, and ring-cleavage-related transformations was proposed; however, the individual product structures were not definitively identified. After five reuse cycles, the TC degradation efficiency remained above 75%, while the degradation selectivity decreased only from 74.7% to 68.7%. NH_2-MIL-101(Fe) also retained preferential TC removal in a TC-spiked domestic wastewater matrix. These results demonstrate that coupling preferential adsorption with localized Fenton-like oxidation provides an effective strategy for enhancing the selective removal of antibiotics from complex aqueous matrices.

Keywords: Fe-MOFs; NH_2-MIL-101(Fe); adsorption-coupled heterogeneous Fenton-like oxidation; antibiotics; tetracycline; selective degradation

Check for updates

Academic Editors: Muhammad Saeed Akhtar and Wajid Zaman

Received: 18 August 2026
Revised: 7 September 2026
Accepted: 7 September 2026
Published: 9 September 2026

Copyright: © 2026 by the authors. Licensee MDPI, Basel, Switzerland. This article is an open access article distributed under the terms and conditions of the Creative Commons Attribution (CC BY) license.

1. Introduction

Antibiotics have been extensively used in human medicine and animal production, and their continuous release has resulted in their frequent detection in aquatic environments [1–3]. Tetracyclines are an important class of broad-spectrum antibiotics and are widely used for the prevention and treatment of infectious diseases [4,5]. Tetracycline (TC), a representative tetracycline antibiotic, is relatively persistent in the environment and difficult to completely remove through conventional treatment processes [6]. Moreover, a substantial fraction of administered TC can be excreted in biologically active forms and subsequently enter wastewater and natural water bodies, potentially promoting the

development and dissemination of antibiotic resistance [7]. Therefore, developing effective technologies for the removal of residual TC from wastewater is of considerable environmental importance [8].

Current technologies for treating TC-containing wastewater mainly include physical, biological, and chemical processes. Adsorption can effectively transfer TC from the aqueous phase to solid adsorbents through various interfacial interactions [9,10]; however, it does not destroy the molecular structure of TC and therefore requires subsequent treatment or regeneration of the adsorbent [11]. Biological treatment is economical for conventional organic wastewater, but the toxicity and relatively low biodegradability of antibiotics may limit their microbial removal. Advanced oxidation processes (AOPs), including photocatalytic oxidation, ozonation, electrocatalytic oxidation, and Fenton oxidation, can generate highly reactive species such as hydroxyl radicals (·OH) and have demonstrated high efficiencies for the degradation of refractory organic pollutants. Li et al. [12] prepared a series of W/CeO_2 composites, achieving a 97.0% Fenton degradation rate for ciprofloxacin within 180 min at pH = 3.0, with ·OH and $\cdot O_2^-$. Nevertheless, the strong oxidation ability of these reactive species is generally accompanied by poor pollutant selectivity. In complex wastewater containing multiple organic constituents, background organic matter may compete with target antibiotics for reactive species, thereby decreasing oxidant utilization efficiency and target-pollutant removal [13].

Among AOPs, Fenton oxidation has received considerable attention because iron species can activate H_2O_2 to generate highly reactive ·OH for the degradation of refractory organic contaminants [14]. In the classical Fenton reaction, Fe^{2+} reacts with H_2O_2 to generate Fe^{3+} and ·OH, while subsequent reactions contribute to Fe^{3+}/Fe^{2+} cycling (Figure 1a). However, conventional homogeneous Fenton systems generally operate efficiently under acidic conditions and may suffer from iron-sludge generation, dissolved-iron discharge, and difficulties in catalyst recovery [15]. Heterogeneous Fenton-like systems have therefore been developed by immobilizing catalytic iron sites on solid materials, facilitating catalyst recovery and reducing iron-related secondary contamination [16]. Despite these advantages, the non-selective consumption of reactive species remains an important limitation. Thus, enhancing the probability of target pollutants reaching catalytic active sites before oxidation may provide an effective strategy for improving degradation selectivity in multicomponent wastewater.

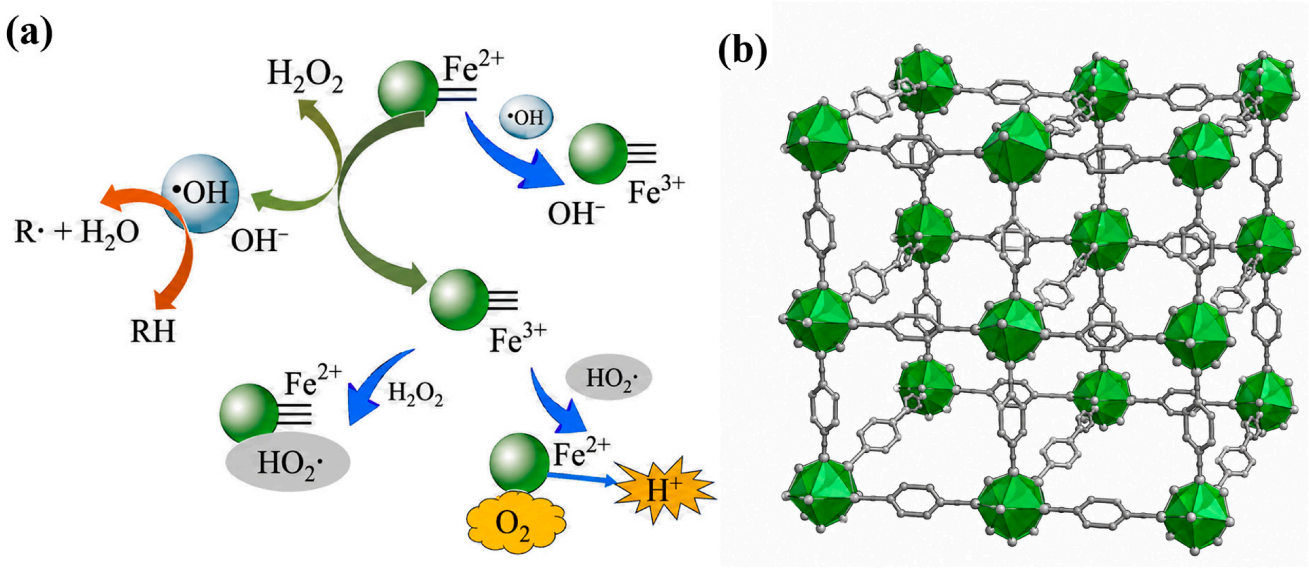


Figure 1. Schematic illustration of (**a**) the Fenton-like reaction mechanism and (**b**) a representative three-dimensional MOF framework composed of metal nodes/clusters and organic linkers.

Metal–organic frameworks (MOFs) are porous coordination networks assembled from metal ions or metal clusters and multitopic organic linkers, forming three-dimensional frameworks with accessible pores and tunable coordination environments (Figure 1b) [17]. Their high porosity, large specific surface areas, tunable pore structures, and accessible active sites make them attractive for adsorption and catalytic applications [18,19]. MOFs and MOF-based materials have consequently been investigated in energy, gas separation, environmental remediation, membrane processes, catalysis, adsorption, and biomedical applications [20–27]. In particular, Fe-based MOFs can combine pollutant adsorption with Fe-mediated H_2O_2 activation, providing a potential platform for coupling pollutant enrichment with heterogeneous Fenton-like oxidation. Their interfacial properties can also be regulated through ligand functionalization or incorporation of additional functional components [28–30]. Fu et al. [31], for example, constructed a TC-imprinted photocatalyst using NH_2-MIL-101(Fe) as a carrier and achieved a TC adsorption capacity of 57.5 mg/g, demonstrating the potential of regulating the interfacial affinity of MOF-based materials toward target antibiotics. Recent studies published in 2026 have further demonstrated the potential of MOF-based materials for TC removal through both adsorption and catalytic degradation. Roozbeh et al. [32] developed amine-functionalized NH_2-ZIF-11 for TC adsorption and showed that amino functionalization enhanced TC uptake through the combined effects of electrostatic interactions, π-π interactions, and hydrogen bonding. Liang et al. [33] constructed a magnetic Fe_3O_4@SiO_2@UiO-66 composite for adsorptive TC removal, demonstrating that structural modification of MOFs can facilitate both pollutant capture and material recovery. In addition to adsorption, MOF-based catalytic systems have recently been developed for oxidative TC degradation. Feng et al. [34] prepared a Ce/Fe-based MOF for Fenton-like photocatalytic degradation of TC, while Sun et al. [35] constructed a g-C_3N_4/MIL101 composite in which Fe sites served as recognition centers for tetracycline antibiotics and promoted their enrichment near catalytic sites prior to photo-Fenton degradation. These studies demonstrate that regulating the surface chemistry, metal centers, and interfacial structure of MOFs can substantially enhance TC adsorption or catalytic degradation. Nevertheless, adsorption-dominated systems mainly transfer TC from the aqueous phase to the solid phase and therefore still require adsorbent regeneration or subsequent treatment, whereas several catalytic systems rely on external light irradiation or relatively complex composite architectures. More importantly, the selective utilization of reactive species for target-antibiotic degradation in the presence of competing organic matter remains insufficiently explored. However, whether the intrinsic adsorption preference of non-imprinted Fe-MOFs can be translated into selective Fenton-like degradation in the presence of competing organic matter remains insufficiently understood.

In this study, MIL-53(Fe), MIL-101(Fe), and NH_2-MIL-101(Fe) were synthesized via a solvothermal method to construct an adsorption-coupled heterogeneous Fenton-like system for selective TC degradation. TC was selected as the target pollutant, while glucose was employed as a competing organic compound to investigate the relationship between adsorption preference and degradation selectivity. Glucose was selected because it is a highly water-soluble and readily biodegradable carbohydrate that can compete with TC for short-lived reactive species such as ·OH. In biological wastewater treatment systems, microorganisms produce extracellular polymeric substances (EPS), which contain substantial polysaccharide and carbohydrate fractions. A recent study of activated sludge collected from wastewater treatment plants worldwide showed that microbial EPS contained appreciable polysaccharide components, while another review reported that microbial exopolysaccharides can contain sugar units such as D-glucose, D-fructose, D-mannose, and related monosaccharides [36,37]. Moreover, microbial communities and EPS are also directly involved in the treatment of tetracycline-containing wastewater; Du et al. reported in 2026 that tetracycline exposure

significantly altered EPS contents and microbial-community characteristics in algal–bacterial granular sludge treating synthetic livestock and poultry wastewater [38]. Therefore, glucose was employed in the present study as a simple and controllable surrogate for readily biodegradable carbohydrate-type organic matter that may coexist with antibiotics and compete for reactive species, rather than as a complete representation of the complex organic composition of actual antibiotic-containing wastewater. The adsorption and selective degradation performances of the three Fe-MOFs were systematically compared, and NH_2-MIL-101(Fe), which exhibited the highest TC degradation selectivity, was further evaluated in terms of reusability and iron leaching. Electron spin resonance and radical scavenging experiments were conducted to identify the dominant reactive species and investigate the location of the oxidation reaction, while LC–MS analysis was used to explore the possible TC degradation pathway. Finally, the catalytic performance of NH_2-MIL-101(Fe) was evaluated in TC-spiked domestic wastewater to examine its behavior in a more complex aqueous matrix. This study focuses on the relationship between preferential interfacial adsorption and selective heterogeneous Fenton-like oxidation, providing a potential strategy for improving the selective removal of antibiotics from multicomponent wastewater.

2. Results and Discussion

2.1. Characterization Analysis

The synthesis procedures of MIL-53(Fe), MIL-101(Fe), and NH_2-MIL-101(Fe) are illustrated in Figure 2a. The SEM images (Figure 2b–g) show that MIL-53(Fe) exhibits a smooth block-like morphology with a length of approximately 5 μm, and numerous impurities are observed, which are speculated to result from the oxidation of iron ions to iron oxides during synthesis. MIL-101(Fe) presents a uniform octahedral morphology with a smooth surface, with diameters ranging from 600 nm to 2 μm. NH_2-MIL-101(Fe) maintains a complete octahedral crystal structure with uniform size (approximately 400 nm in diameter), indicating that amination does not disrupt the original crystal structure of NH_2-MIL-101(Fe).

XRD characterization was employed to investigate the crystal structures of the materials. As shown in Figure 3a, the characteristic diffraction peaks of MIL-53(Fe), MIL-101(Fe), and NH_2-MIL-101(Fe) are consistent with those reported in the literature, confirming the successful synthesis of these materials [39–41]. The infrared spectrum of MIL-53(Fe) (Figure 3b) confirms the presence of carboxyl groups and aromatic rings. Compared with MIL-101(Fe), NH_2-MIL-101(Fe) exhibits characteristic peaks of amino groups, indicating successful introduction of amino functional groups. The characteristic peaks of the three materials show no obvious changes before and after adsorption, demonstrating their structural stability. Additionally, in the NH_2-MIL-101(Fe) reaction system, amino functionalization provides additional hydrogen-bonding sites and modifies the surface electronic environment of NH_2-MIL-101(Fe), which may enhance its interfacial affinity toward TC through multiple interactions, including hydrogen bonding, π-π interactions, and electrostatic interactions.

The N_2 adsorption–desorption isotherms of the three materials (Figure 3c–e) are typical Type IV isotherms, confirming their mesoporous structures. The specific surface areas of MIL-53(Fe), MIL-101(Fe), and NH_2-MIL-101(Fe) are 31.2 m^2/g, 304 m^2/g, and 248 m^2/g, respectively. A larger specific surface area provides more adsorption sites to facilitate pollutant adsorption by the catalyst. When the relative pressure is less than 0.8, the adsorption isotherms rise gradually, indicating the presence of micropores. When the relative pressure exceeds 0.8, the N_2 adsorption capacity increases rapidly, suggesting uniformly distributed mesopores with interconnected channels that are beneficial for physical adsorption. As shown in Table 1, MIL-101(Fe) has a larger specific surface area

and pore diameter than MIL-53(Fe), which is conducive to mass transfer and diffusion of pollutants within its pore channels. The relatively low BET surface area of MIL-53(Fe) (31.2 m^2/g) may be related to the flexible "breathing" behavior of its framework, which can lead to narrow-pore configurations and limited N_2 accessibility during adsorption measurements. Similar relatively low surface areas have also been reported for pristine MIL-53(Fe) materials [42]. The specific surface area of NH_2-MIL-101(Fe) decreases significantly after introducing amino groups, possibly due to its larger average pore diameter (4.90 nm) compared to MIL-101(Fe) (3.71 nm).

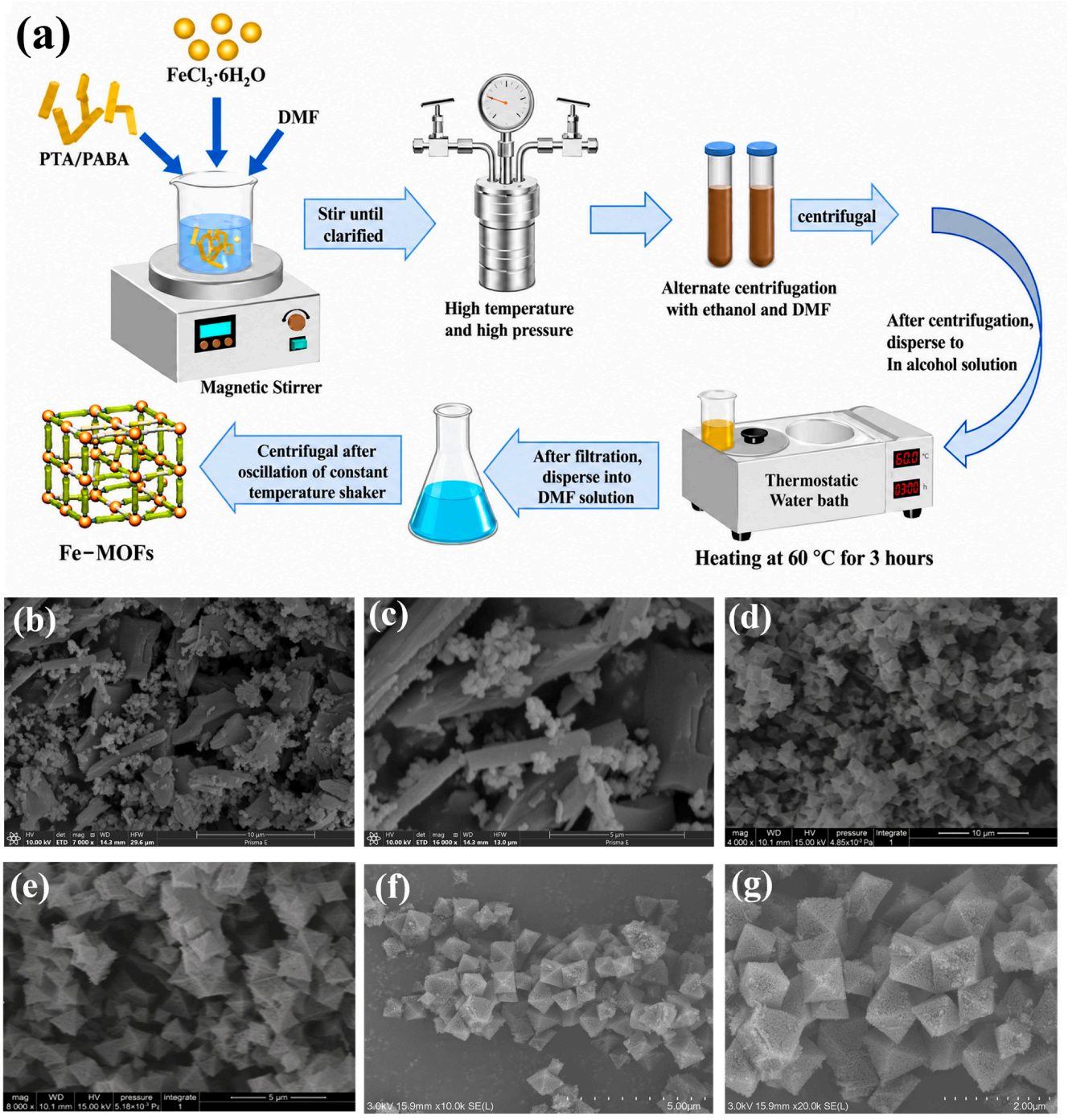


Figure 2. (**a**) Flowchart of the preparation of MIL-53(Fe), MIL-101(Fe) and NH_2-MIL-101(Fe); SEM of sample (**b**) MIL-53(Fe) magnification 7000 times (**c**) MIL-53(Fe) magnification 16,000 times (**d**) MIL-101(Fe) magnification 4000 times (**e**) MIL-101(Fe) magnification 8000 times (**f**) NH_2-MIL-101(Fe) magnification 10,000 times (**g**) NH_2-MIL-101(Fe) amplification 20,000 times.

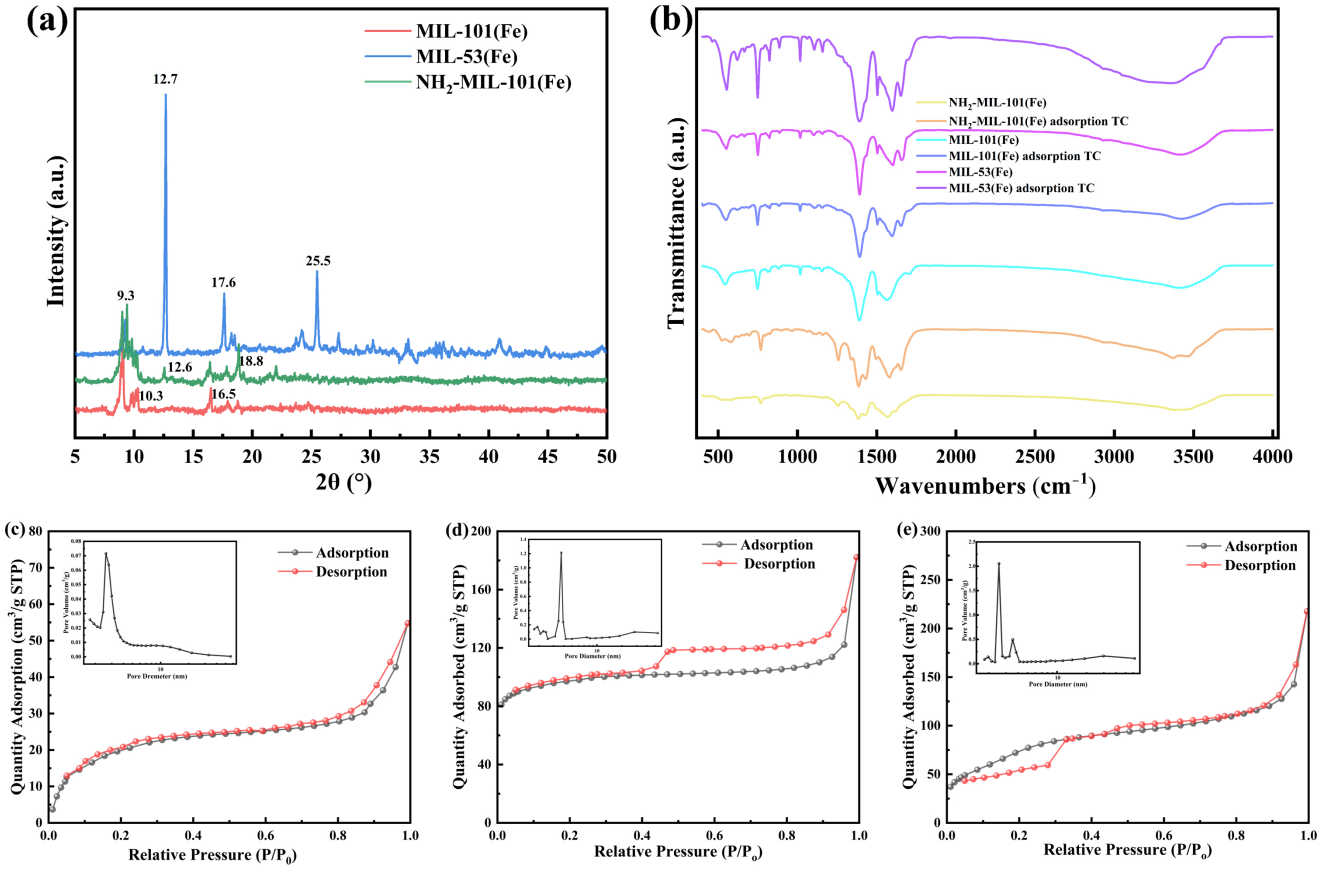


Figure 3. (**a**) XRD pattern of synthesized materials; (**b**) Infrared spectra of synthesized materials; N2 adsorption and desorption isotherms of (**c**) MIL-53(Fe), (**d**) MIL-101(Fe) and (**e**) NH_2-MIL-101(Fe).

Table 1. Specific surface area, pore volume, and pore diameter of MIL-53(Fe), MIL-101(Fe), and NH_2-MIL-101(Fe).

	Specific Surface Area (m^2/g)	Pore Volume (cm^3/g)	Pore Diameter (nm)
MIL-53(Fe)	31.2	0.030	3.86
MIL-101(Fe)	304	0.282	3.71
NH_2-MIL-101(Fe)	248	0.337	4.90

XPS was used to analyze the chemical state of elements. The XPS survey spectra (Figure 4a) of all three materials exhibit the characteristic peaks of C 1s, O 1s, and Fe 2p. The high-resolution N 1s spectrum of NH_2-MIL-101(Fe) (Figure S5) shows a characteristic peak centered at approximately 400.0 eV, which is attributed to the amino nitrogen (-NH_2) of the organic linker, further demonstrating the presence of amino functionalities in the framework. The high-resolution C 1s spectra (Figure 4b) can be deconvoluted into three components centered at approximately 284.8, 286.1, and 288.5 eV, which are assigned to C-C/C=C, C-O or C-N, and O-C=O, respectively. The peak near 286.1 eV is markedly enhanced in NH_2-MIL-101(Fe), mainly owing to the formation of C-N bonds. The O 1s spectra (Figure 4c) were deconvoluted into three components centered at approximately 529.6, 531.8, and 533.5 eV, which can be assigned to Fe-O-related oxygen, carboxylate oxygen in the Fe-O-C coordination environment, and surface hydroxyl groups and/or adsorbed water, respectively. The component near 531.8 eV is the major contribution in the three Fe-MOFs, consistent with the abundant carboxylate-coordinated oxygen in their frameworks. Differences in the relative contributions of the O 1s components among the three materials reflect variations in their local surface oxygen environments. As shown in

Figure 4d, the Fe 2p spectra exhibit two main peaks at approximately 711.9 and 725.2 eV, corresponding to Fe $2p_{3/2}$ and Fe $2p_{1/2}$, respectively. A characteristic shake-up satellite feature is also observed between the two main Fe 2p peaks. These spectral features are consistent with Fe being predominantly present in an Fe(III)-containing coordination environment in the three Fe-MOFs. Since the exact Fe 2p binding energies may vary slightly with the local coordination environment, surface charging, and spectral fitting, the small differences among the three materials were not interpreted as direct evidence of changes in Fe oxidation state.

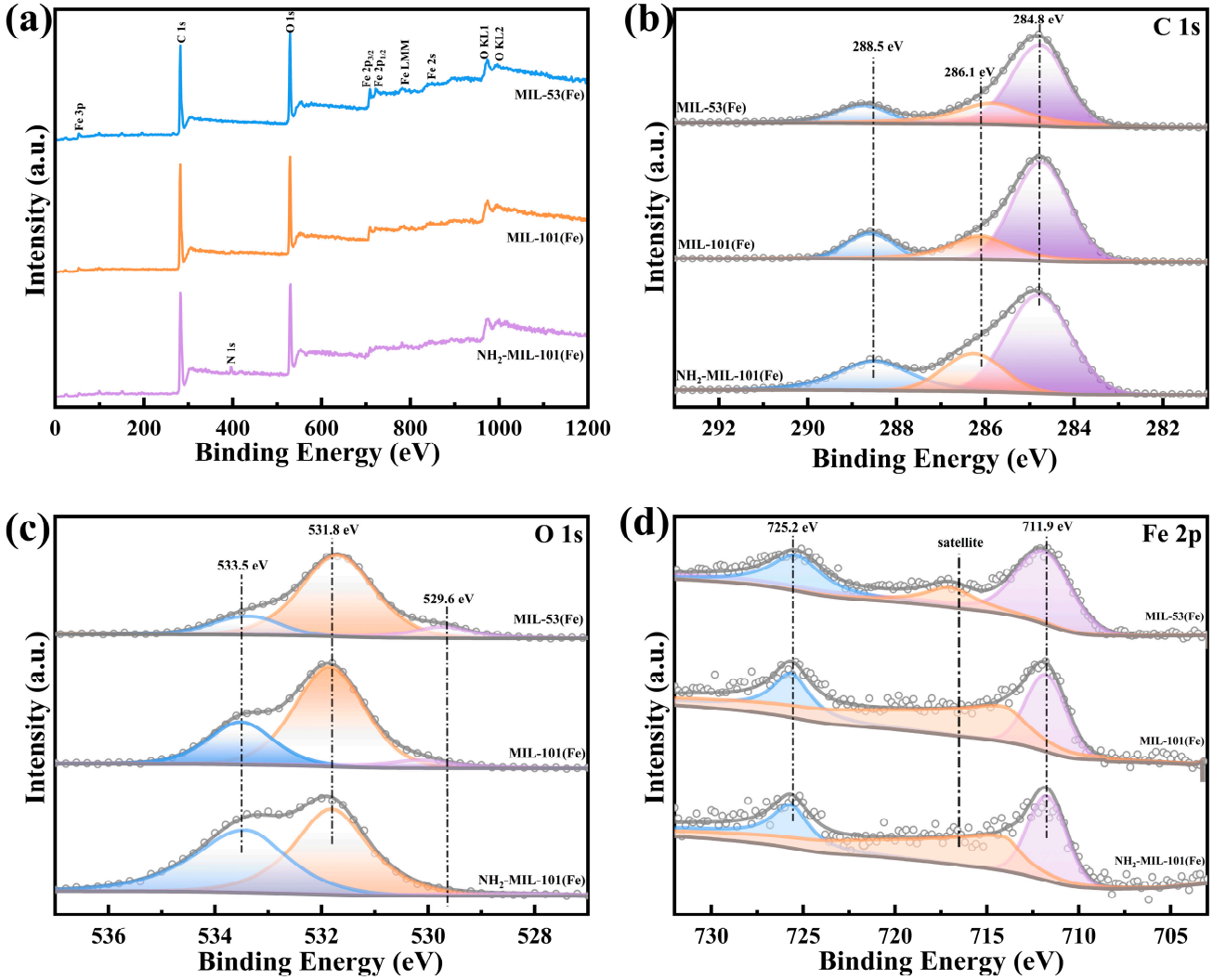


Figure 4. (**a**) XPS survey spectra of synthesized materials; (**b**) C 1 s spectra; (**c**) O 1 s spectra; (**d**) Fe 2p spectra.

Zeta potential measurements (Figure S6a) showed that MIL-53(Fe) exhibited a negatively charged surface when dispersed in aqueous solution, whereas MIL-101(Fe) and NH_2-MIL-101(Fe) were positively charged. Notably, the zeta potential of NH_2-MIL-101(Fe) was markedly higher than that of MIL-101(Fe), which may be attributed to the protonation of amino groups, resulting in positively charged -NH_3^+ species in aqueous solution. Furthermore, the pH-dependent zeta potential measurements of NH_2-MIL-101(Fe) revealed that its surface remained positively charged at pH < 8, while the zeta potential (Figure S6b) gradually decreased with increasing solution pH. The surface approached electrical neutrality at pH 8–9, indicating that the point of zero charge (pH_pzc) was located within this range. At pH > 9, the surface charge of NH_2-MIL-101(Fe) became negative.

2.2. Adsorption Performance of MOFs for TC

2.2.1. Adsorption Isotherms

The equilibrium adsorption behavior of TC on the three MOFs was evaluated using the Langmuir and Freundlich adsorption isotherm models. As shown in Figure 5a,c,e and Table 2, the adsorption of TC onto MIL-53(Fe) was better described by the Langmuir model, suggesting a relatively more homogeneous distribution of effective adsorption sites. In contrast, the Freundlich model provided better fits for MIL-101(Fe) and NH_2-MIL-101(Fe), indicating greater heterogeneity in adsorption-site energies. The satisfactory fits obtained with both models suggest that TC adsorption cannot be fully described by a single idealized adsorption mode and may involve multiple interfacial interactions.

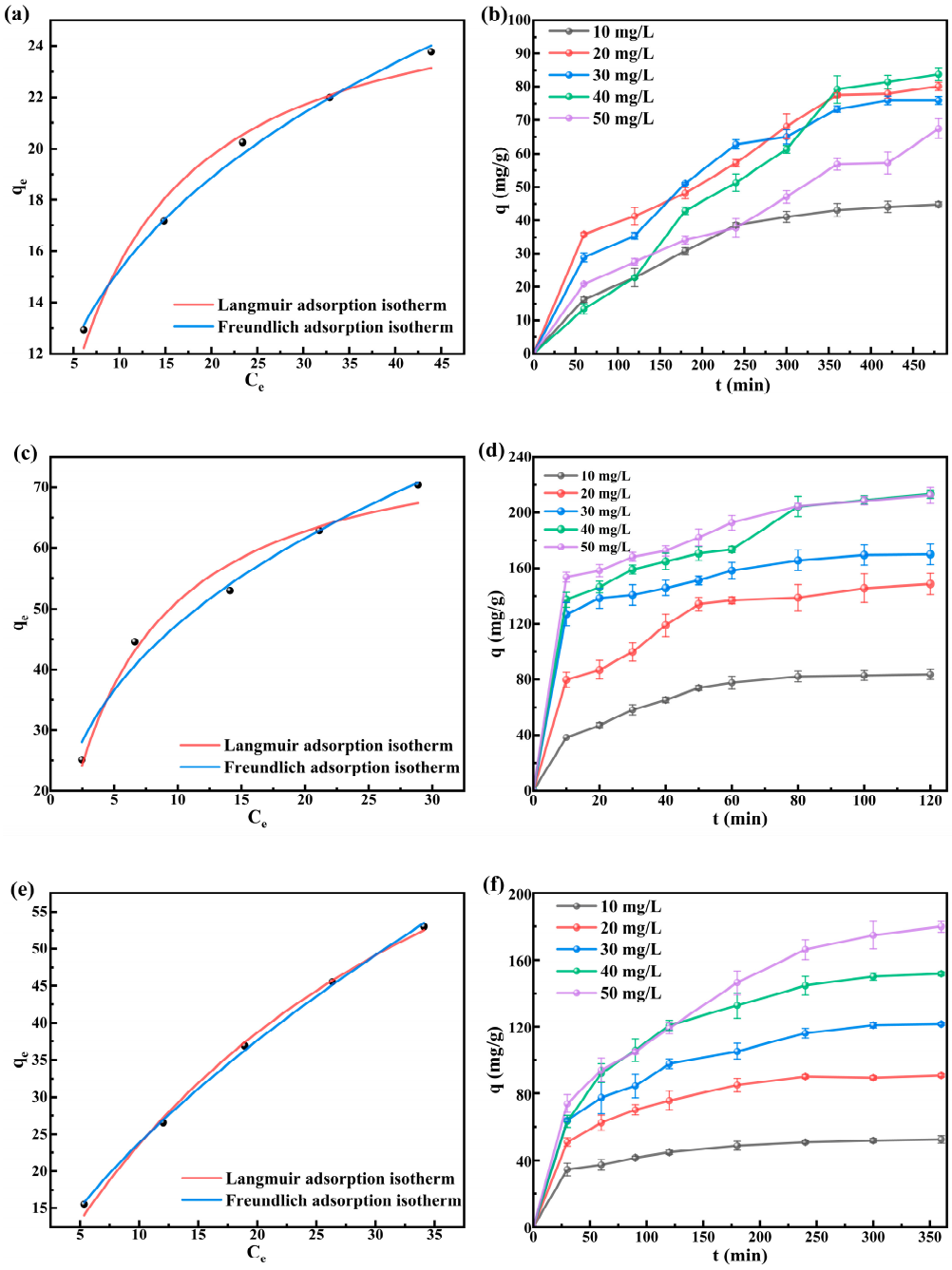


Figure 5. Adsorption isotherm fitting of (**a**) MIL-53 (Fe), (**c**) MIL-101 (Fe) and (**e**) NH_2-MIL-101 (Fe) for TC; (**b**) MIL-53(Fe), (**d**) MIL-101(Fe), (**f**) NH_2-MIL-101(Fe) Adsorption kinetics of TC.

Table 2. Relevant parameters for langmuir and freundlich adsorption isotherm fitting of TC by Fe-MOFs.

	Langmuir Equation	q_{max}	K_L	R^2
MIL-53	$y = 3.6375x/(1 + 0.1344x)$	27.065	0.1344	0.9951
MIL-101	$y = 13.9021x/(1 + 0.1715x)$	81.061	0.1715	0.9659
NH_2-MIL-101	$y = 3.0393x/(1 + 0.0285x)$	106.642	0.0285	0.9966
	Freundlich equation	1/n	K_F	R^2
MIL-53	$y = 7.5283x^{0.3067}$	0.3067	7.5283	0.9683
MIL-101	$y = 19.938x^{0.3767}$	0.3767	19.938	0.9797
NH_2-MIL-101	$y = 5.2252x^{0.6590}$	0.6590	5.2252	0.9989

Frontier molecular orbital analysis was further performed to evaluate the electronic characteristics of TC. As shown in Figure 6a,b, the highest occupied molecular orbital (HOMO) and lowest unoccupied molecular orbital (LUMO) are unevenly distributed over the TC molecular skeleton and are mainly localized around the O^- and N-containing functional groups and their adjacent conjugated structures. The calculated HOMO and LUMO energies are −5.74 and −2.35 eV, respectively, corresponding to a HOMO–LUMO energy gap (ΔE) of 3.39 eV. The HOMO-enriched regions represent relatively electron-rich portions of the TC molecule and therefore constitute potential electron-donating sites for interfacial interactions, whereas the LUMO distribution reflects regions with relatively higher electron-accepting capability. Together with the molecular structure shown in Figure S7a, these results indicate that the carbonyl, hydroxyl, amide, and dimethylamino groups and their adjacent conjugated structures constitute electronically active regions that may participate in the interfacial adsorption of TC onto Fe-MOFs. However, these molecular-orbital distributions identify potential interaction sites rather than directly demonstrating a specific Fe–TC coordination configuration.

The Fukui f^- distribution (Figure 6c), which describes the local susceptibility toward electrophilic attack, further reveals the heterogeneous electron-donating character of different regions of the TC molecule and complements the HOMO analysis in identifying potentially electron-rich interaction sites.

2.2.2. Adsorption Kinetics

Regarding the influence of adsorption time and initial concentration on the adsorption capacity of TC by different catalysts—i.e., the adsorption kinetics of MOFs—Figure 5b,d,f shows that for MIL-53(Fe), MIL-101(Fe), and NH_2-MIL-101(Fe), the adsorption capacity of TC increased relatively rapidly within the first 300 min, 60 min, and 180 min, respectively, in TC solutions of different initial concentrations. As adsorption time prolonged, the adsorption rate decreased significantly, and the adsorption capacity approached equilibrium. This phenomenon can be attributed to the abundance of empty adsorption sites on the MOF surface at the initial stage, combined with a large concentration gradient between TC in the solution and on the catalyst, which facilitates rapid adsorption. As adsorption proceeded, TC occupied most adsorption sites, the TC concentration in the solution decreased, the driving force of the concentration gradient diminished, and the diffusion rate of TC molecules within the catalyst slowed, making adsorption more difficult until a dynamic equilibrium between adsorption and desorption was achieved. MIL-53(Fe), MIL-101(Fe), and NH_2-MIL-101(Fe) reached adsorption equilibrium at 360 min, 240 min, and 180 min, respectively. Notably, MIL-101(Fe) exhibited the best adsorption performance and the fastest equilibrium attainment, with a saturation adsorption capacity of 39.03 mg/g for 20 mg/L TC, followed by NH_2-MIL-101(Fe) (52.45 mg/g), while MIL-53(Fe) showed the poorest performance (41.06 mg/g) and the longest equilibrium time. The possible reason is

that the large specific surface area of MIL-101(Fe) provides more adsorption sites, which are conducive to TC adsorption.

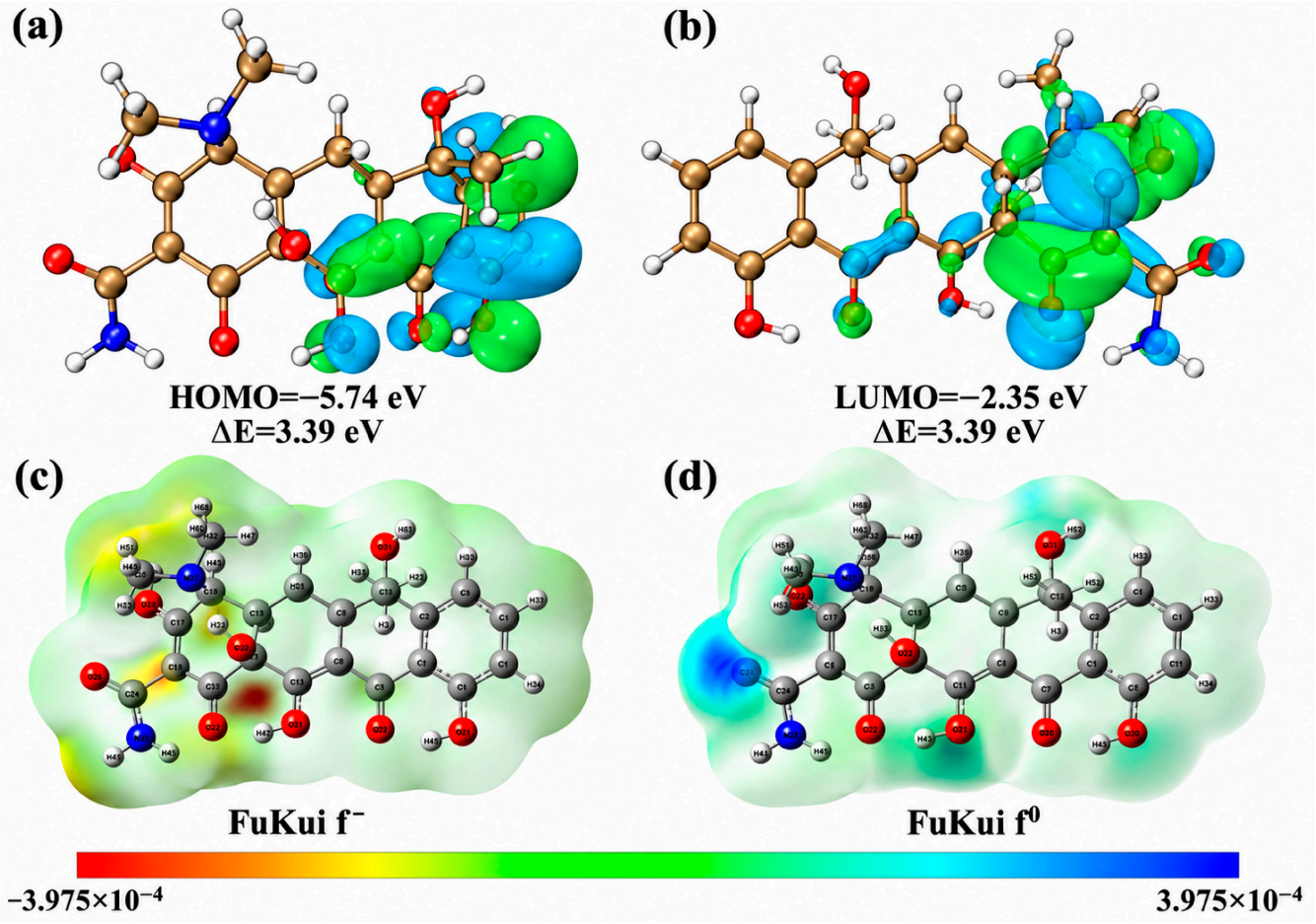


Figure 6. Frontier molecular orbitals and Fukui-function distributions of tetracycline (TC): (**a**) HOMO; (**b**) LUMO; (**c**) Fukui f^- distribution for electrophilic attack; and (**d**) Fukui f^0 distribution for radical attack. The calculated HOMO and LUMO energies are −5.74 and −2.35 eV, respectively, with a HOMO–LUMO energy gap (ΔE) of 3.39 eV.

To compare the kinetic behavior of TC adsorption on the three Fe-MOFs, the experimental data were fitted using the pseudo-first-order and pseudo-second-order models. As shown in Figure 7 and Table S1, the pseudo-second-order model generally gave higher correlation coefficients (R^2) than the pseudo-first-order model, indicating that it provides a better empirical description of the adsorption kinetics. However, kinetic-model fitting alone is insufficient to establish a unique adsorption mechanism or to demonstrate that chemisorption is the dominant process. Therefore, the kinetic results are interpreted primarily as empirical descriptions of the adsorption behavior, while the overall adsorption process may involve multiple interfacial interactions and mass-transfer steps.

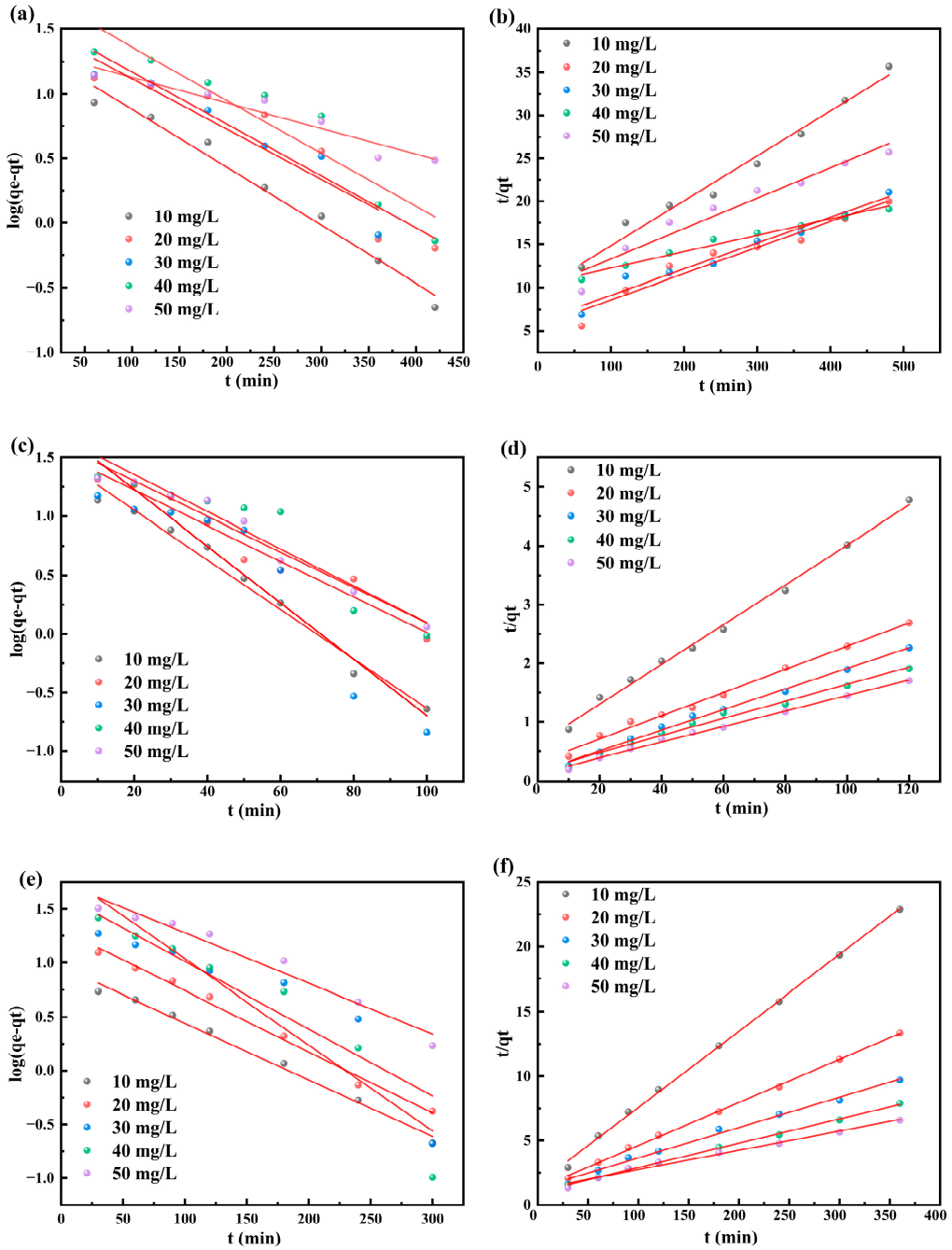


Figure 7. (**a**) Pseudo-first-order kinetic fitting curves of MIL-53(Fe), (**c**) MIL-101(Fe), and (**e**) NH_2-MIL-101(Fe) for TC adsorption; (**b**) pseudo-second-order kinetic fitting curves of MIL-53(Fe), (**d**) MIL-101(Fe), and (**f**) NH_2-MIL-101(Fe) for TC adsorption.

2.3. Selective Degradation of Tetracycline (TC) in Simulated Wastewater by MOFs

In terms of the selective degradation results of MOFs, as the glucose concentration increased, the degradation rate of TC by MIL-53(Fe) gradually decreased. When the glucose concentration was 10 mg/L, the TC degradation rate was 78.9%; as the glucose concentration increased to 50 mg/L, the TC removal rate dropped to 52.5%. At this point, the catalyst degraded 28.87 × 10^{-3} mmol of glucose, but only 7.09 × 10^{-3} mmol of TC (Figure 8a,b), and the degradation selectivity for TC decreased from 47.3% to 19.7% (Figure 8c). Similar to MIL-53(Fe), the TC degradation capacity of MIL-101(Fe) was also inhibited with increasing glucose concentration (Figure 8d,e). The degradation rate decreased from 91.4% to 77.8%, the TC degradation amount dropped from 12.4 × 10^{-3} mmol to 10.6 × 10^{-3} mmol, the

glucose degradation amount increased from 7.1 × 10^{-3} mmol to 20.4 × 10^{-3} mmol, and the degradation selectivity for TC decreased from 63.5% to 34.2% (Figure 8f). When the TC-to-glucose concentration ratio was 2/2, the catalyst degraded 10.7 × 10^{-3} mmol of TC and 10.6 × 10^{-3} mmol of glucose, with a TC degradation selectivity of 50.2%. For NH_2-MIL-101(Fe) (Figure 8g,h), as the glucose concentration increased, the TC degradation rate decreased from 85.3% to 81.6%, the TC degradation amount dropped from 11.52 × 10^{-3} mmol to 11.02 × 10^{-3} mmol, the glucose degradation amount increased from 2.91 × 10^{-3} mmol to 9.01 × 10^{-3} mmol, and the degradation selectivity for TC decreased from 79.8% to 55.0% (Figure 8i). When the TC-to-glucose concentration ratio was 2/2, the catalyst degraded 10.36 × 10^{-3} mmol of TC and 3.86 × 10^{-3} mmol of glucose, with a TC degradation selectivity of 73.1%.

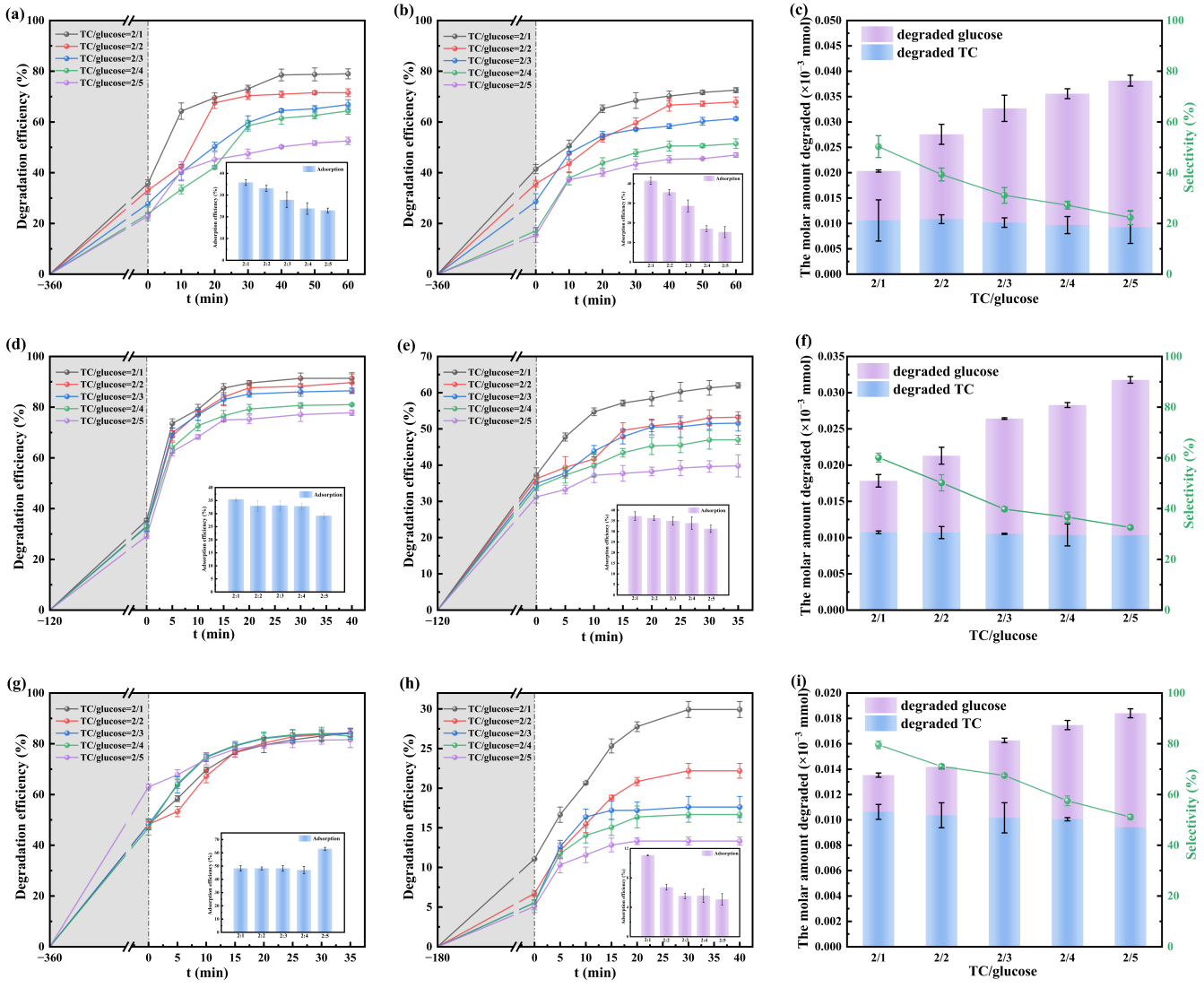


Figure 8. Influence of initial concentration ratio of TC to glucose on the selective degradation performance of Fe-MOFs catalysts. (**a**) TC degradation rate, (**b**) glucose degradation rate and (**c**) degradation selectivity of MIL-53(Fe); (**d**) TC degradation rate, (**e**) glucose degradation rate, and (**f**) degradation selectivity of MIL-101(Fe); (**g**) TC degradation rate, (**h**) glucose degradation rate and (**i**) degradation selectivity of NH_2-MIL-101(Fe).

Among the three catalysts, the final TC degradation rates followed the order: MIL-101(Fe) > NH_2-MIL-101(Fe) > MIL-53(Fe), and their TC degradation rates were all higher than those for glucose. The degradation selectivity for TC followed the order: NH_2-MIL-

101(Fe) > MIL-101(Fe) > MIL-53(Fe), which is consistent with their selective adsorption performance for TC. This indicates that the degradation pathway of TC by these three catalysts involves two steps: first, the pollutants are adsorbed onto the catalyst surface; then, H_2O_2 in the solution is catalyzed by iron ions on the catalyst to generate ·OH radicals, which degrade the adsorbed pollutants on the catalyst surface. Additionally, the Fenton-like degradation selectivity of all three catalysts was higher than that of the adsorption system without H_2O_2, possibly because in the Fenton-like system, the adsorbed TC and glucose molecules are degraded and desorbed, keeping the adsorption active sites on the catalyst in an unsaturated state. The catalyst then re-adsorbs TC and glucose molecules, and as shown in Figure S8, the adsorption capacity of MIL-101(Fe) and NH_2-MIL-101(Fe) for TC is greater than that for glucose. Although the TC degradation performance of MIL-101(Fe) is significantly better than that of MIL-53(Fe), the addition of glucose still significantly inhibits TC degradation, consistent with the changes observed in the simple adsorption system. NH_2-MIL-101(Fe) exhibited notably higher degradation selectivity for TC than the other two catalysts. Therefore, the term "selective degradation" used in this work describes preferential pollutant-level removal of TC relative to glucose, which is attributed to preferential interfacial enrichment of TC before oxidation.

By comparing the COD concentrations of the NH_2-MIL-101(Fe) system before and after degradation in the TC-glucose mixed solution (concentration ratio TC/glucose concentration ratio of 2:2) and the single TC solution, it was found that in the single TC system, the COD values before and after degradation were 56.1 mg/L and 24.2 mg/L, respectively, with a COD removal rate of 56.9% after heterogeneous Fenton-like degradation by NH_2-MIL-101(Fe), indicating that TC was almost completely degraded within 40 min, which validates the rationality of the degradation process. In the two-component system, the COD values before and after degradation were 77.2 mg/L and 41.1 mg/L, respectively, with a degradation rate of 46.8%. Assuming the inhibitory effect of glucose on TC degradation is negligible (Figure 8g), approximately 4.95 mg/L of the degraded COD in the two-component system originated from glucose degradation. Although the parent TC was largely transformed, the COD removal of 56.9% indicated only partial mineralization and the persistence of organic intermediates, and that from glucose was 23.5%, further confirming the superior degradation selectivity of NH_2-MIL-101(Fe) for TC. The COD was determined according to the method described in Supplementary Text S4.

2.4. Reusability and Stability of NH_2-MIL-101(Fe)

The reusability and stability of catalysts are critical indicators for evaluating their performance. In the adsorption experiments (Figure 9a,b), after five cycles of use, the TC removal rate decreased from 43.9% to 28.1%, and the glucose removal rate decreased from 7.2% to 5.9%, both showing a continuous decline. Although the catalyst was regenerated via ethanol-assisted ultrasonic washing between cycles, the gradual decline in adsorption performance may indicate that a fraction of strongly adsorbed TC-derived intermediates was not completely removed during regeneration, resulting in progressive occupation or blockage of accessible adsorption sites. It should be noted that the adsorption and degradation stages in each reuse cycle were sequentially conducted in the same reaction system. After the adsorption stage reached equilibrium, H_2O_2 was directly added to initiate the Fenton-like degradation reaction. Accordingly, t = 0 in Figure 9c,d represents the moment of H_2O_2 addition rather than the beginning of the entire adsorption–degradation experiment. Because a fraction of TC and glucose had already been removed during the preceding adsorption stage, the overall removal efficiencies at t = 0 were greater than zero. The subsequent increase in removal efficiency reflects the additional removal achieved after activation of H_2O_2. During the subsequent Fenton-like degradation stage (Figure 9c,d),

the overall TC removal efficiency remained above 75.0% after five cycles, indicating that NH_2-MIL-101(Fe) still exhibits good degradation performance for TC. The degradation selectivity for TC slightly decreased from 74.7% to 68.7% (Figure S9). Additionally, the iron ion concentration in the solution was very low during the reuse of NH_2-MIL-101(Fe), with only minimal iron leaching (Figure 9e,f), demonstrating the material's certain reusability. Taken together, the performance of NH_2-MIL-101(Fe) in both adsorption and degradation reuse experiments indicates that the catalyst has high recyclability and stability.

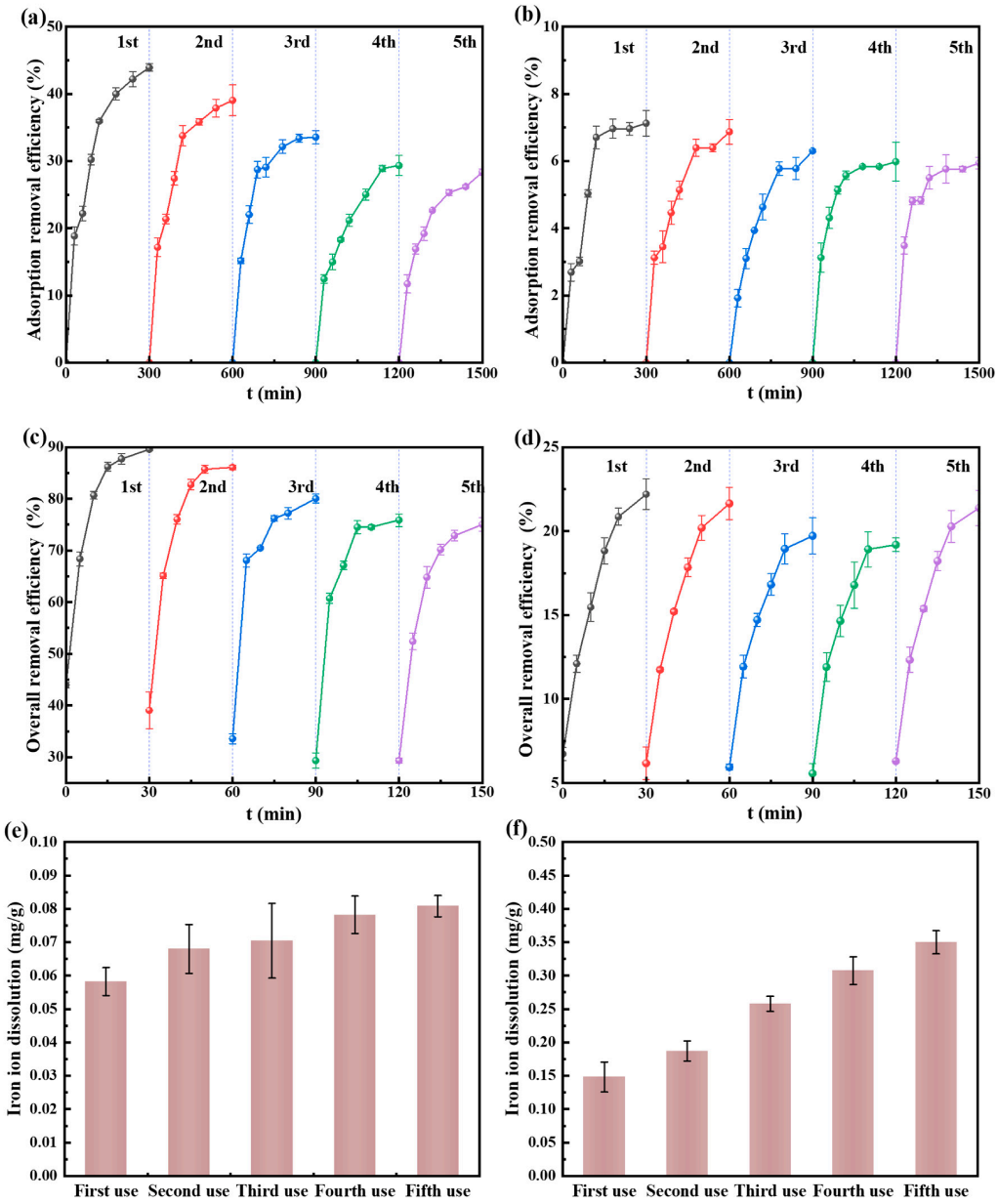


Figure 9. Reusability and stability of NH_2-MIL-101(Fe) during sequential adsorption–degradation cycles: adsorption removal efficiencies of (**a**) TC and (**b**) glucose; overall removal efficiencies of (**c**) TC and (**d**) glucose after H_2O_2 addition following adsorption equilibrium; iron leaching during repeated (**e**) adsorption and (**f**) degradation experiments. For panels (**c**) and (**d**), t = 0 corresponds to the moment of H_2O_2 addition after adsorption equilibrium, and the initial non-zero removal represents pollutant removal achieved during the preceding adsorption stage.

In the stability study, the iron ion leaching amount during the adsorption process was below 0.08 mg/g (Figure 9e), almost negligible. During five reuse cycles (Figure 9f), the iron ion leaching amounts in the solution were 0.147 mg/g, 0.187 mg/g, 0.258 mg/g,

0.297 mg/g, and 0.350 mg/g, with an average of 0.247 mg/g. These results show that iron ions on the NH_2-MIL-101(Fe) catalyst are well preserved after degradation reactions. These relatively low Fe-leaching amounts indicate limited loss of framework Fe during repeated operation and suggest a low risk of Fe-related secondary contamination.

2.5. Identification of Reactive Species and Radical Scavenging Experiments

To characterize the reactive oxygen species generated in the NH_2-MIL-101(Fe)/H_2O_2 system, ESR measurements were performed using DMPO as the spin-trapping agent. Because free ·OH has an extremely short lifetime, it was not detected directly; instead, ·OH was trapped by DMPO to form the relatively longer-lived DMPO-OH spin adduct. As shown in Figure 10a, the experimental ESR spectrum exhibited a characteristic four-line signal with an approximately 1:2:2:1 intensity pattern. The hyperfine splitting constants were determined to be aN ≈ aH ≈ 14.9 G, with a calculated g value of approximately 2.0061, consistent with the characteristic parameters reported for the DMPO-OH spin adduct [43,44].

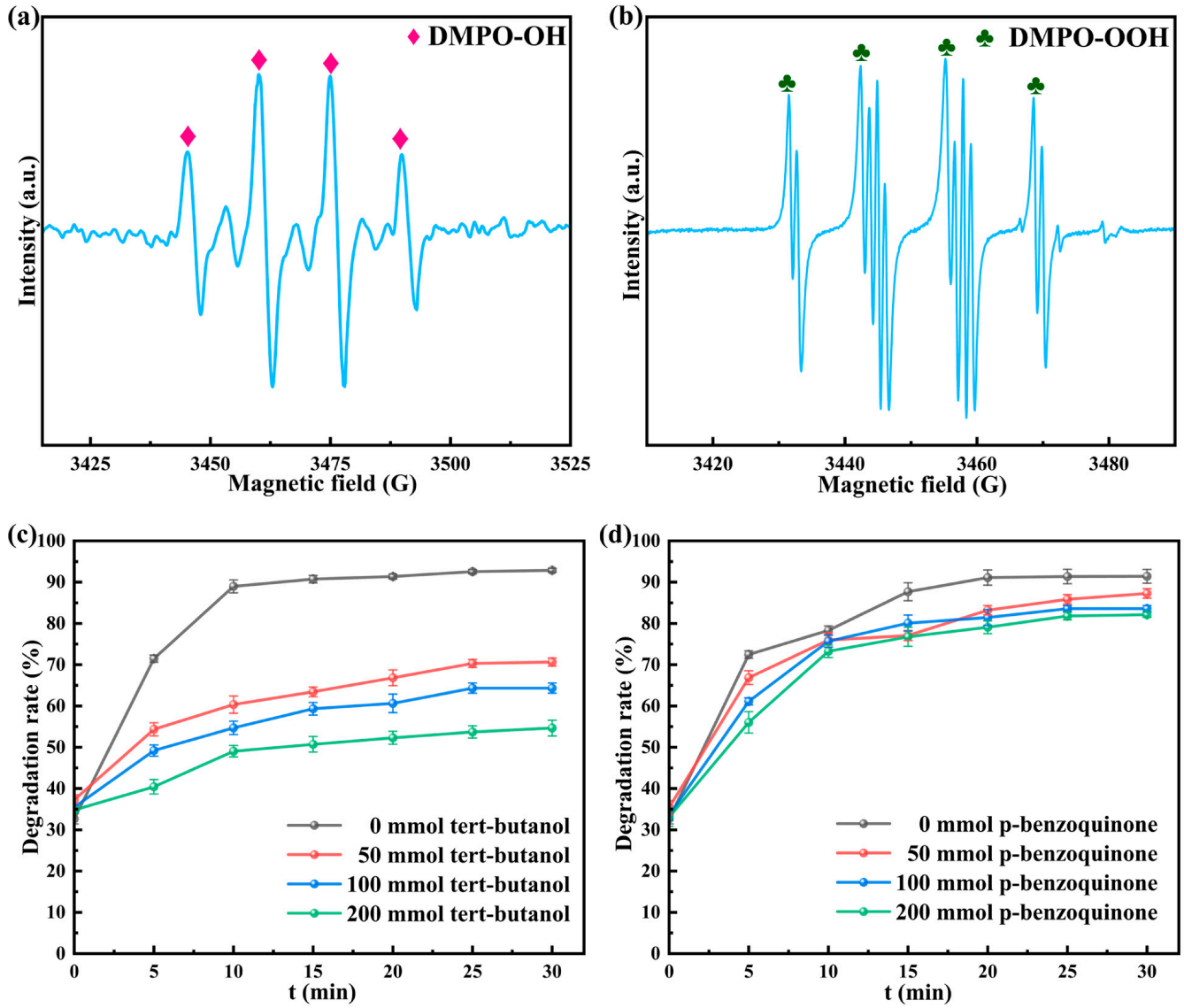


Figure 10. ESR spectra of DMPO spin adducts generated in the NH_2-MIL-101(Fe)/H_2O_2 system: (**a**) DMPO-OH, indicating ·OH generation, and (**b**) DMPO-OOH, associated with superoxide/hydroperoxyl species; effects of radical scavengers on TC degradation: (**c**) tert-butanol and (**d**) p-benzoquinone.

For superoxide-related species, the experimentally measured ESR spectrum in Figure 10b exhibited the characteristic multiline pattern of the DMPO-OOH spin adduct. The experimental magnetic-resonance parameters were g ≈ 2.0058, aN ≈ 13.1 G, aHβ ≈ 10.7 G, and aHγ ≈ 1.2 G. These values are comparable to previously reported parameters for DMPO-OOH spin adducts [45,46], supporting the formation of superoxide/hydroperoxyl-related species in the NH_2-MIL-101(Fe)/H_2O_2 system. However, ESR spin trapping confirms the presence of these radical species but does not independently determine their relative contributions to TC degradation. Therefore, radical-scavenging experiments were further performed to identify the dominant reactive species.

As shown in the results, after adding 50 mmol/L tert-butanol (a scavenger for ·OH), the degradation efficiency of TC decreased from 92.8% (without scavenger) to 70.6% after 10 min of reaction. Moreover, the degradation efficiency of TC gradually declined with the increase of tert-butanol concentration, and only reached 54.7% when the concentration was raised to 200 mmol/L (Figure 10c). In contrast, the addition of p-benzoquinone (a scavenger for $\cdot O_2^-$) exerted a slight influence on the catalytic activity of NH_2-MIL-101(Fe) (Figure 10d). This indicates that ·OH acts as the dominant active species during the heterogeneous Fenton-like degradation of TC over NH_2-MIL-101(Fe), while $\cdot O_2^-$ plays a negligible role.

KI is a radical scavenger that can capture ·OH on the catalyst surface, which helps determine whether the degradation reaction mainly occurs on the catalyst surface or in the bulk solution. Figure S10 shows that the TC degradation efficiency was 70.8% with the addition of 50 mmol/L KI. When the KI concentration increased to 100 mmol/L, the degradation efficiency dropped sharply from 93.4% (0 mmol/L KI) to 46.2%, presenting a stronger inhibitory effect than tert-butanol. Consequently, the TC degradation process over NH_2-MIL-101(Fe) is a heterogeneous Fenton-like reaction dominated by ·OH radicals, which primarily takes place on the catalyst surface.

2.6. Proposed Adsorption–Degradation Mechanism of NH_2-MIL-101(Fe)

As an efficient environmental remediation material, the NH_2-MIL-101(Fe) catalyst exhibits excellent performance in treating wastewater containing tetracycline antibiotics due to its unique structural and chemical properties [47]. The abundant amino (-NH_2) functional groups on its surface enable NH_2-MIL-101(Fe) to adsorb TC molecules in water selectively. Surface Fe sites are proposed to mediate Fe^{3+}/Fe^{2+} redox cycling, through which H_2O_2 is activated to produce ·OH [48]. Owing to their strong oxidizing ability, hydroxyl radicals rapidly oxidize and degrade the TC adsorbed on the catalyst surface. As the reaction proceeds, degradation products desorb from the catalyst surface, releasing new active sites. Due to the catalyst's high activity and stability, this desorption process is reversible: TC in the solution is re-adsorbed onto the catalyst surface and then degraded again. This cyclic mechanism of adsorption–degradation–re-adsorption–re-degradation enhances the TC removal efficiency (Figure 11a).

Transformation-related ions generated during TC degradation in the NH_2-MIL-101(Fe)/H_2O_2 system were analyzed via full-scan LC–MS in positive electrospray ionization mode (ESI+) after 30 and 60 min of reaction. The parent TC ion was observed at m/z 445.07, together with several lower-mass signals, including m/z 430.73–430.75, 417.21, 300.86–300.91, 261.12, and 219.90–220.78 (Figure S11 and Table S2). On the basis of the nominal m/z values and chemically plausible oxidative reactions of TC, P1 and P2 were tentatively associated with possible N-demethylation-related transformations. In contrast, the signals designated as P3–P5 were treated more conservatively as tentative transformation ions because their specific molecular formulas and structures could not be unambiguously established from the available full-scan LC–MS data. These ions

may be associated with subsequent oxidative fragmentation and/or ring-cleavage-related processes, but such assignments remain hypothetical. These assignments are proposed only as one chemically plausible interpretation of the detected signals and should not be regarded as definitive structural identifications. We also re-examined the complete full-scan spectra and noted several signals with m/z values higher than that of the parent TC, extending to approximately m/z 702. These high-mass signals were not included in the proposed pathway because their molecular identities cannot be reliably determined from the available full-scan MS data. They may originate from different ionization-related, association, condensation/oligomerization, or matrix-related processes, but the present data are insufficient to distinguish among these possibilities. Therefore, these signals are explicitly reported as unassigned high-mass ions rather than being forced into the proposed degradation sequence. Because neither MS/MS fragmentation spectra nor high-resolution accurate-mass and NMR data were available, Figure 11b is explicitly presented as a tentative transformation scheme rather than a confirmed degradation pathway. Accordingly, the LC-MS results are used here only to support the occurrence of TC transformation and to propose possible reaction routes, rather than to establish unique molecular structures.

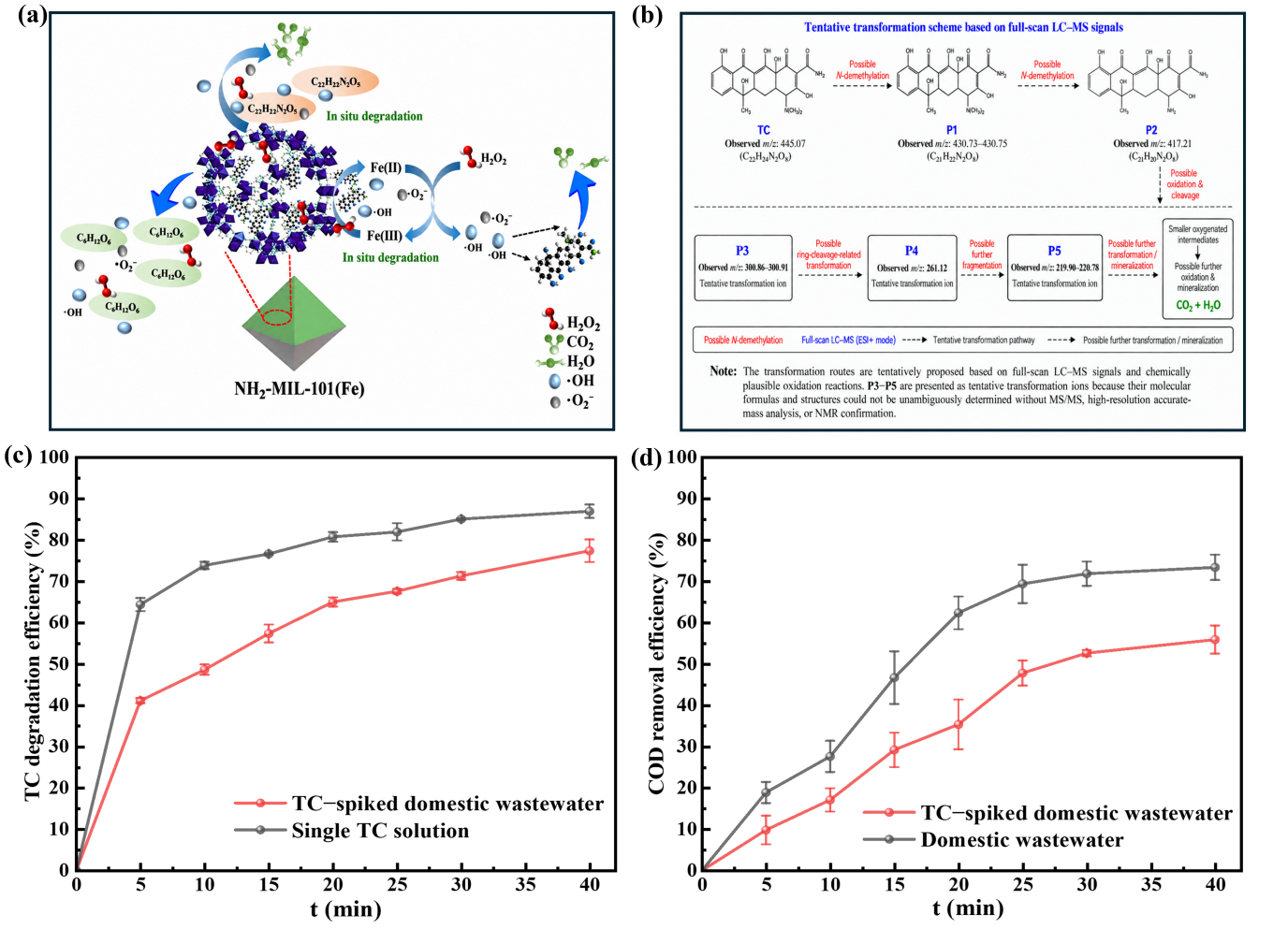


Figure 11. (**a**) Proposed selective degradation mechanism; (**b**) Tentative transformation scheme of TC based on full-scan LC-MS signals in the NH_2-MIL-101(Fe)/H_2O_2 system; (**c**) TC degradation efficiency in the single TC solution and TC-spiked domestic wastewater; (**d**) COD removal efficiency in domestic wastewater and TC-spiked domestic wastewater.

Quantum-chemical calculations further provide molecular-level support for the proposed TC degradation mechanism. As shown in Figure 6a,b, the HOMO and LUMO of TC

exhibit pronounced spatial heterogeneity, indicating that the electronic activity is not uniformly distributed over the molecular skeleton. More importantly, Fukui-function analysis was employed to evaluate the local reactivity of TC toward different types of chemical attack. The f^0 distribution (Figure 6d), which reflects susceptibility toward radical attack, shows that the radical reactivity of TC is concentrated in specific regions rather than being uniformly distributed throughout the molecule. These reactive regions are mainly associated with O^- and N-containing functional groups and their adjacent conjugated structures [49].

This prediction is consistent with the experimental identification of ·OH as the dominant reactive species and with the pronounced inhibition observed after KI addition, indicating that TC oxidation occurs predominantly at or near the NH_2-MIL-101(Fe) surface. The predicted radical-sensitive regions provide qualitative chemical plausibility for some of the transformations tentatively proposed from the LC-MS data; however, the Fukui-function analysis cannot independently confirm the structures of the detected transformation ions. In contrast, the f^- distribution shown in Figure 6c mainly reflects electron-donating regions, while the complementary f^+ distribution is provided in Figure S7b. Taken together, the frontier molecular orbital, Fukui-function, radical-scavenging, and LC–MS results support a mechanism in which TC is first preferentially enriched near surface Fe sites and subsequently subjected to localized ·OH attack.

2.7. Practical Application of NH_2-MIL-101(Fe) in Domestic Wastewater and TC-Spiked Domestic Wastewater

The performance of NH_2-MIL-101(Fe) was further evaluated in three aqueous matrices: a single TC solution, filtered domestic wastewater, and TC-spiked domestic wastewater. The domestic wastewater was collected from a domestic wastewater discharge area near Xuanwu Lake, Xuanwu District, Nanjing, Jiangsu Province, China. In the single TC solution (Figure 11c), TC degradation proceeded rapidly during the initial 5 min and reached 87.0% after 30 min, corresponding to a degraded TC amount of 5.85 mg.

For the filtered domestic wastewater, the COD removal efficiency reached 73.4% after 30 min (Figure 11d), corresponding to a COD removal amount of 38.19 mg (Figure S12). In the TC-spiked domestic wastewater, the presence of background organic constituents inhibited the overall oxidation process. Nevertheless, TC was still preferentially removed relative to the coexisting organic matter, indicating that NH_2-MIL-101(Fe) retained its preferential TC-removal capability in a more complex wastewater matrix.

In the TC-spiked domestic wastewater, COD removal was inhibited by the presence of coexisting organic constituents. After 30 min, the COD removal efficiency reached 55.9%, corresponding to a COD removal amount of 33.88 mg. During the initial 5 min, TC degradation reached 41.1% (2.77 mg), whereas COD removal was only 8.1% (5.11 mg), indicating that TC was transformed more rapidly than the bulk organic constituents during the early reaction stage. This preferential TC removal may be associated with its interfacial enrichment on NH_2-MIL-101(Fe). At the end of the reaction, 5.21 mg of TC was degraded in the TC-spiked domestic wastewater, slightly lower than the 5.85 mg degraded in the single TC solution, indicating that background organic constituents competed with TC for reactive sites and reactive species.

3. Materials and Methods

3.1. Materials

All reagents used in the experiment were of analytical grade. Terephthalic acid was purchased from Shanghai Linen Technology Development Co., Ltd. (Shanghai, China). Anhydrous glucose, N,N-dimethylformamide, 30% hydrogen peroxide, and 1,10-phenanthroline were obtained from Sinopharm Chemical Reagent Co., Ltd. (Shanghai,

China). 2-Aminoterephthalic acid, iron(III) chloride hexahydrate, ethanol, TC, phenol, and hydroxylamine hydrochloride were supplied by Shanghai Macklin Biochemical Technology Co., Ltd. (Shanghai, China). Concentrated sulfuric acid, hydrochloric acid, sodium acetate anhydrous, and acetic acid (glacial acetic acid) were purchased from Nanjing Chemical Reagent Co., Ltd. (Nanjing, China).

3.2. Preparation of MOFs

Three Fe-MOFs were prepared using the solvothermal method.

MIL-53(Fe): Terephthalic acid (0.615 g) was dissolved in 56 mL of N,N-dimethylformamide (DMF) under magnetic stirring for 30 min. $FeCl_3 \cdot 6H_2O$ (0.674 g) was then added, and the mixture was further stirred for 5 min until complete dissolution. The resulting solution was transferred into a Teflon-lined autoclave and heated at 150 °C for 24 h. After cooling to room temperature, the product was collected by centrifugation (4000 rpm, 15 min) and alternately washed with absolute ethanol and DMF. The washed solid was immersed in hot absolute ethanol at 60 °C for 3 h, collected by vacuum filtration, and subsequently dispersed in excess DMF and shaken at 25 °C and 160 rpm for 48 h. The solid was then recovered by centrifugation and dried at 70 °C to obtain MIL-53(Fe) [39].

MIL-101(Fe): Terephthalic acid (0.675 g) was dissolved in 15 mL of DMF and stirred for 15 min, followed by the addition of 0.206 g of $FeCl_3 \cdot 6H_2O$. After stirring for another 5 min, the mixture was transferred into a 50 mL Teflon-lined autoclave and heated at 110 °C for 20 h. After cooling, the product was collected by centrifugation (4000 rpm, 15 min), alternately washed with absolute ethanol and DMF, and immersed in hot absolute ethanol at 60 °C for 3 h. The solid was then collected by vacuum filtration, dispersed in excess DMF, and shaken overnight at 25 °C and 160 rpm. After centrifugation, the resulting solid was dried at 70 °C and finally activated at 150 °C for 8 h to obtain MIL-101(Fe) [40].

NH_2-MIL-101(Fe): NH_2-MIL-101(Fe) was prepared using the same procedure as MIL-101(Fe), except that 0.675 g of 2-aminoterephthalic acid was used as the organic ligand and the amount of $FeCl_3 \cdot 6H_2O$ was adjusted to 0.225 g. The resulting dark-brown solid was subjected to the same washing, solvent-exchange, drying, and activation procedures as MIL-101(Fe) [40].

The obtained materials were characterized via X-ray diffraction (XRD), scanning electron microscopy (SEM), Brunauer–Emmett–Teller (BET) specific surface area analysis, Fourier transform infrared spectroscopy (FT-IR), X-ray photoelectron spectroscopy (XPS), and zeta potential measurements.

3.3. Adsorption Performance Test

Before the adsorption experiments, the initial solution pH was adjusted to 7.0. No further pH adjustment or buffer was applied during the adsorption process.

Using TC as a model organic contaminant, the adsorption behavior of TC onto the three MOFs was investigated through adsorption isotherms (Langmuir [50] and Freundlich [51] models) and kinetics (pseudo-first-order and pseudo-second-order equations [52]). For the adsorption isotherm experiments, the initial TC concentrations were set at 10, 20, 30, 40, and 50 mg/L, while the MOF dosage was maintained at 0.3 g/L. The TC concentration was determined via UV-Vis spectrophotometry according to Supplementary Text S1. Samples with TC concentrations exceeding 30 mg/L were appropriately diluted with deionized water before analysis to ensure that the measured concentrations remained within the calibration range.

The adsorption data were fitted using two adsorption isotherm models, Langmuir (Equation (1)) and Freundlich (Equation (2)).

$$q_e = \frac{q_{max} K_L C_e}{1 + K_L C_e} \quad (1)$$

$$q_e = K_F C_e^{1/n} \quad (2)$$

where C_e is the equilibrium TC concentration in solution (mg/L); q_e and $q_{\max}$ are the equilibrium and maximum adsorption capacities (mg/g), respectively; K_L is the Langmuir adsorption constant; K_F is the Freundlich adsorption constant; and $1/n$ is the Freundlich heterogeneity factor.

For the adsorption kinetic mechanism, fitting was performed using the pseudo-first-order and pseudo-second-order kinetic equations. The pseudo-first-order kinetic equation is expressed as:

$$\log(q_e\text{-}q_t) = \log q_e\text{-}k_1 t \quad (3)$$

where q_e and q_t are the adsorption capacities of the catalyst for TC at equilibrium and at time t (mg/g), respectively; k_1 is the first-order kinetic constant (min^{-1}).

The pseudo-second-order kinetic equation is expressed as:

$$\frac{t}{q_t} = \frac{1}{k_2 q_{e^2}} + \frac{t}{q_e} \quad (4)$$

where q_e and q_t are the adsorption capacities of TC at equilibrium and at time t (mg/g), respectively; k_2 is the second-order kinetic constant ($\text{g}\cdot\text{mg}^{-1}\cdot\text{min}^{-1}$).

For the linearized pseudo-second-order model, t/q_t was plotted against t. The fitted equilibrium adsorption capacity was calculated as $q_e = 1/\text{slope}$, and the pseudo-second-order rate constant was obtained according to $k_2 = 1/(\text{intercept} \times q_e^2)$.

3.4. Selective Degradation of TC over MOFs

Using glucose as a competing organic compound, 150 mL of TC solution (40 mg/L) was mixed with 150 mL of glucose solution (20, 40, 60, 80, or 100 mg/L) in a 500 mL Erlenmeyer flask, giving a total aqueous reaction volume of 300 mL. After mixing, the final TC concentration in the reaction system was 20 mg/L, while the final glucose concentrations were 10, 20, 30, 40, and 50 mg/L, respectively, corresponding to TC/glucose concentration ratios of 2:1, 2:2, 2:3, 2:4, and 2:5. This concentration design allowed the concentration of the target pollutant to remain constant while systematically increasing the concentration of the competing organic compound, thereby providing different degrees of competitive interference for evaluating the selective adsorption and degradation performance of the three Fe-MOFs toward TC. The TC concentration was determined according to Supplementary Text S1, and samples with TC concentrations above 30 mg/L were diluted with deionized water prior to UV–Vis analysis to ensure that the measured concentrations fell within the calibration range. Before adsorption, the initial pH of the mixed solution was adjusted to 7.0. No further pH adjustment was performed after H_2O_2 addition, and no buffer was used during the reaction. After adding 0.3 g/L of the three MOFs, the mixtures were shaken in a thermostatic shaking incubator at 25 °C and 200 rpm until adsorption equilibrium was reached. All adsorption and degradation experiments were conducted under normal laboratory lighting conditions, without deliberate dark treatment or additional external light irradiation. Subsequently, 20 mmol/L H_2O_2 was added, and samples were collected at regular intervals to determine the concentrations of TC and glucose (Glucose concentration was determined according to the method described in Supplementary Text S2), thereby evaluating the selective degradation capability of the MOFs.

In this study, the selectivity of the catalyst was defined as the molar amount of the target pollutant adsorbed or degraded relative to the total molar amount of pollutants adsorbed or degraded, as expressed by the following equation:

$$Selectivity(\%) = \frac{n_{target}}{n_{target} + n_{interferent}} \times 100\% \quad (5)$$

where n_{target} and $n_{interferent}$ represent the molar amounts of the target pollutant and interfering pollutant adsorbed or degraded, respectively. A higher selectivity value indicates a stronger preference of the catalyst for the target pollutant.

It should be emphasized that "degradation selectivity" in this study refers to the preferential degradation of TC relative to the coexisting competing organic compound (glucose), as quantitatively defined by Equation (5). It does not imply that ·OH selectively attacks a specific chemical bond or molecular position within TC.

3.5. Reusability and Stability Studies

The reusability and stability of NH_2-MIL-101(Fe) were investigated using a TC/glucose concentration ratio of 2:2. Specifically, 150 mL of TC solution (40 mg/L) was mixed with 150 mL of glucose solution (40 mg/L), resulting in a total reaction volume of 300 mL and final concentrations of 20 mg/L for both TC and glucose. The NH_2-MIL-101(Fe) dosage was 0.3 g/L. After adsorption equilibrium was reached, H_2O_2 was added to a final concentration of 20 mmol/L. The time at which H_2O_2 was added was defined as t = 0 for the degradation stage. Because the degradation experiment directly followed the adsorption-equilibrium stage, the pollutant removal at t = 0 reflected the removal already achieved by adsorption. Upon completion of each reaction cycle, the MOF particles were recovered by vacuum filtration and subsequently washed with deionized water by centrifugation. The recovered catalyst was then dispersed in heated ethanol and ultrasonicated for 40 min to remove residual pollutants and degradation intermediates adsorbed on the catalyst surface and within the pores. After ultrasonication, the catalyst was separated by centrifugation and alternately washed with deionized water and ethanol three times. The regenerated catalyst was then dried at 75 °C for 6 h before being reused in the subsequent cycle. This recovery and regeneration procedure was repeated for five consecutive cycles. Meanwhile, the iron leaching concentration in the solution after each reuse was determined to assess the material stability. The iron ion concentration was determined according to the method described in Supplementary Text S3.

3.6. Evaluation in Domestic Wastewater and TC-Spiked Domestic Wastewater

Domestic wastewater was collected from a domestic wastewater discharge area near Xuanwu Lake, Xuanwu District, Nanjing, Jiangsu Province, China. A total of 3000 mL of domestic wastewater was collected and filtered through a 0.45 μm membrane before use. The filtered wastewater had an initial pH of approximately 6.4 and a COD concentration of 173.5–185.7 mg/L.

To prepare the TC-spiked domestic wastewater, 30 mg of TC was added to 1500 mL of the filtered domestic wastewater and thoroughly mixed, giving a final TC concentration of 20 mg/L. The COD concentration of the resulting TC-spiked domestic wastewater was 204.4–231.8 mg/L.

Three aqueous matrices were evaluated: a single TC solution (20 mg/L), filtered domestic wastewater, and TC-spiked domestic wastewater. For each experiment, 300 mL of the corresponding water sample was transferred into a 500 mL Erlenmeyer flask. NH_2-MIL-101(Fe) was added at a dosage of 0.4 g/L, followed by H_2O_2 to a final concen-

tration of 20 mmol/L. Samples were collected at 5 min intervals to determine TC and COD concentrations.

3.7. Fukui Function Calculations

The condensed Fukui functions (f^-, f^+, and f^0) were calculated to evaluate the local reactivity of different atomic sites in the TC molecule toward electrophilic, nucleophilic, and radical attacks, respectively. The Fukui functions for atom A were calculated according to Equations (6)–(8):

$$f_A^- = q_{N-1}^A - q_N^A \quad (6)$$

$$f_A^+ = q_N^A - q_{N+1}^A \quad (7)$$

$$f_A^0 = \left(q_{N-1}^A - q_{N+1}^A\right)/2 \quad (8)$$

where q_N^A, q_{N+1}^A, and q_{N-1}^A represent the atomic charges of atom A in the neutral, one-electron-added (anionic), and one-electron-removed (cationic) states of TC, respectively. N represents the total number of electrons in the neutral TC molecule, and A denotes a specific atom in the molecule. The f_A^- value describes the susceptibility of atom A toward electrophilic attack, f_A^+ reflects its susceptibility toward nucleophilic attack, and f_A^0 represents its susceptibility toward radical attack. In general, a larger positive Fukui-function value indicates a more reactive atomic site toward the corresponding type of chemical attack.

The molecular structure of TC was calculated using Gaussian 16. The electronic-structure calculations were performed using the B3LYP functional with the 6-31G basis set, and the atomic charges of the neutral, anionic, and cationic states were used to calculate the corresponding Fukui-function values.

3.8. Statistical Analysis

Unless otherwise stated, all batch adsorption, degradation, radical-scavenging, and reuse experiments were independently performed in triplicate (n = 3). The results are presented as the mean ± standard deviation (SD), and the error bars in the corresponding figures represent the standard deviation of three independent experiments.

3.9. Characterization and Analysis

BET: The textural properties of the samples were characterized by N_2 adsorption–desorption measurements using an ASAP-2020 surface area and pore-size analyzer (Micromeritics, Norcross, GA, USA). Prior to analysis, the samples were dried at 80 °C for 8 h. N_2 adsorption–desorption isotherms were recorded, and the corresponding surface-area and pore-structure parameters were calculated from the adsorption data; the pore-size distribution was evaluated using the BJH method.

SEM: The surface morphology of the samples was examined using a JSM-7600F field-emission scanning electron microscope (JEOL Ltd., Tokyo, Japan). Before observation, the dried powder samples were sputter-coated with Au to improve electrical conductivity. The elemental composition of the samples was additionally examined via energy-dispersive X-ray spectroscopy (EDS) when required.

FT-IR: Fourier-transform infrared spectra were recorded using a Nicolet iS5 FT-IR spectrometer (Thermo Fisher Scientific, Waltham, MA, USA) in attenuated total reflectance (ATR) mode using dried powder samples.

XRD: X-ray diffraction patterns were obtained using an Ultima IV X-ray diffractometer (Rigaku Corporation, Tokyo, Japan). The diffraction patterns were recorded over a 2θ range of 5–50° at a scanning rate of 5° min^{-1}.

XPS: X-ray photoelectron spectroscopy (XPS) measurements were performed using an AXIS Ultra DLD spectrometer (Kratos Analytical Ltd., Manchester, UK) equipped with a monochromatic Al Kα X-ray source. Survey spectra were collected over a binding-energy range of 0–1200 eV, and high-resolution spectra of C 1s, O 1s, Fe 2p, and, for NH_2-MIL-101(Fe), N 1s were further recorded for analysis of the surface chemical states.

Zeta potential: Zeta potentials were measured using a Zetasizer Nano ZS analyzer (Malvern Instruments Ltd., Malvern, UK). The samples were dispersed in deionized water and ultrasonicated for 40 min to obtain homogeneous suspensions. An appropriate amount of each suspension was transferred into the measurement cell and analyzed at room temperature. Each measurement was independently repeated three times.

ESR: Reactive oxygen species were characterized using a Micro electron spin resonance spectrometer (Bruker BioSpin GmbH, Rheinstetten, Germany), with DMPO employed as the spin-trapping agent. For ·OH detection, the microwave power was 10 mW, the microwave frequency was 9.740168 GHz, and the magnetic field was swept from 3360 to 3570 G using 1680 acquisition points and 10 accumulated scans at approximately 35 °C. The experimental DMPO-OH spectrum exhibited a characteristic four-line pattern with $g \approx 2.0061$ and $aN \approx aH \approx 14.9$ G. For superoxide-related species, the experimentally measured DMPO-OOH spectrum exhibited a characteristic multiline pattern with $g \approx 2.0058$, $aN \approx 13.1$ G, $aH\beta \approx 10.7$ G, and $aH\gamma \approx 1.2$ G.

LC-MS: The degradation intermediates of TC were analyzed using an Auto Purification HPLC/MS system (Waters Corporation, Milford, MA, USA) in positive electrospray ionization mode (ESI+), with a full-scan range of m/z 50–750.

4. Conclusions

Three Fe-MOFs, MIL-53(Fe), MIL-101(Fe), and NH_2-MIL-101(Fe), were synthesized and evaluated for adsorption-coupled selective degradation of TC. TC adsorption on MIL-53(Fe) was better described by the Langmuir model, whereas TC adsorption on MIL-101(Fe) and NH_2-MIL-101(Fe) showed better agreement with the Freundlich model, indicating differences in the distribution and heterogeneity of their adsorption sites. In the binary TC/glucose system, the overall TC degradation efficiency followed the order MIL-101(Fe) > NH_2-MIL-101(Fe) > MIL-53(Fe), whereas the degradation selectivity followed the order NH_2-MIL-101(Fe) > MIL-101(Fe) > MIL-53(Fe). At a TC/glucose concentration ratio of 2:2, NH_2-MIL-101(Fe) achieved a TC degradation selectivity of 73.1%, demonstrating that the highest catalytic activity did not necessarily correspond to the highest target-pollutant selectivity.

The selective behavior of NH_2-MIL-101(Fe) was associated with preferential adsorption of TC followed by localized oxidation at the catalyst interface. ESR and scavenging experiments confirmed the generation of ·OH and $\cdot O_2^-$, with ·OH making the dominant contribution to TC degradation. The pronounced inhibition caused by KI further indicated that the reaction occurred predominantly at or near the catalyst surface. Full-scan LC–MS analysis revealed several transformation-related ions, allowing a tentative transformation scheme involving possible N-demethylation, oxidative fragmentation, and ring-cleavage-related processes to be proposed. Frontier molecular orbital and Fukui-function analyses further identified electronically active and radical-sensitive regions of TC, providing molecular-level support for the proposed surface-localized adsorption–oxidation pathway. These results support an adsorption–degradation–re-adsorption cycle in which preferential enrichment of TC near surface Fe sites increases its probability of reacting with short-lived ·OH species.

NH_2-MIL-101(Fe) retained a TC degradation efficiency above 75% after five reuse cycles, while its degradation selectivity decreased from 74.7% to 68.7%, indicating reasonable

catalytic durability. The low iron leaching further suggested limited loss of framework Fe during repeated operation. In the TC-spiked domestic wastewater matrix, competing organic constituents partially suppressed TC oxidation but did not eliminate its preferential degradation. Overall, the results demonstrate that regulating pollutant adsorption at the catalyst interface can improve the effective utilization of locally generated reactive species and thereby enhance degradation selectivity in multicomponent wastewater. Further studies using authentic antibiotic-containing wastewater, together with systematic evaluation of solution pH, matrix constituents, long-term structural stability, and H_2O_2 utilization efficiency, are required to establish the practical applicability of this strategy.

Supplementary Materials: The following supporting information can be downloaded at: https://www.mdpi.com/article/10.3390/catal16090814/s1, Text S1: Determination of TC Concentration; Text S2: Determination of Glucose Concentration; Text S3: Determination of Iron Ion Concentration; Text S4: Determination of Chemical Oxygen Demand (COD); Figure S1: TC concentration curve; Figure S2: Glucose concentration curve; Figure S3: Iron content standard curve; Figure S4: COD concentration standard curve; Figure S5: N 1s spectra of NH_2-MIL-101(Fe); Figure S6: Zeta potential of (a) Fe-MOFs and (b) NH_2-MIL-101(Fe) in different pH solutions; Figure S7: Molecular structure and Fukui f^+ distribution of tetracycline (TC): (a) molecular structure of TC and (b) Fukui f^+ distribution for nucleophilic attack; Figure S8: Influence of initial concentrations on TC adsorption removal efficiency: (a) MIL-53(Fe), (c) MIL-101(Fe), and (e) NH_2-MIL-101(Fe), and effects of initial concentrations on glucose adsorption removal efficiency: (b) MIL-53(Fe), (d) MIL-101(Fe), and (f) NH_2-MIL-101(Fe); Figure S9: Effect of reuse cycles on the selective degradation of TC by NH_2-MIL-101(Fe); Figure S10: Effect of potassium iodide addition on TC removal efficiency; Figure S11: Full-scan LC–MS spectra obtained during TC degradation in the NH_2-MIL-101(Fe)/H_2O_2 system after (a) 30 min and (b) 60 min; Figure S12: TC degradation and COD removal in the single TC solution, domestic wastewater, and TC-spiked domestic wastewater treated with NH_2-MIL-101(Fe); Table S1: Relevant parameters for kinetic model fitting of TC adsorption by MIL-53(Fe), MIL-101(Fe), and NH_2-MIL-101(Fe); Table S2: Tentative assignment of transformation-related ions detected during TC degradation in the NH_2-MIL-101(Fe)/H_2O_2 system by full-scan LC–MS in ESI positive-ion mode; Table S3: Experimental ESR parameters of DMPO spin adducts in the NH_2-MIL-101(Fe)/H_2O_2 system and comparison with reported values. References [53–56] are cited in the Supplementary Materials.

Author Contributions: Methodology, P.Z. and J.H. (Jinzhao Hu); Formal analysis, J.H. (Jinzhao Hu) and J.H. (Jiaxin Hou); Data curation, P.Z.; Writing—original draft, J.H. (Jinzhao Hu) and J.L.; Project administration, J.H. (Jiaxin Hou) and J.L. All authors have read and agreed to the published version of the manuscript.

Funding: This research received no external funding.

Data Availability Statement: All data generated or analyzed during this study are included in this article.

Acknowledgments: The authors sincerely thank all individuals who contributed to the successful completion of this experimental research and express their deep gratitude for all the contributions of the researchers. They are particularly grateful to all of their collaborators, supporters, and colleagues who provided valuable opinions, comprehensive knowledge content, feasible research plans, and unwavering support for the experiment.

Conflicts of Interest: The authors declare no conflicts of interest.

Abbreviations

The following abbreviations are used in this manuscript:

AOPs	Advanced oxidation processes
BET	Brunauer–Emmett–Teller
COD	Chemical oxygen demand

DMF	N,N-Dimethylformamide
ESR	Electron spin resonance
Fe-MOFs	Iron-based metal–organic frameworks
FT-IR	Fourier transform infrared spectroscopy
HOMO	Highest occupied molecular orbital
LC–MS	Liquid chromatography–mass spectrometry
LUMO	Lowest unoccupied molecular orbital
MOFs	Metal–organic frameworks
ROS	Reactive oxygen species
SEM	Scanning electron microscopy
TC	Tetracycline
XPS	X-ray photoelectron spectroscopy
XRD	X-ray diffraction

References

1. Xu, Y.; Gao, H.; Li, R.; Lou, Y.; Li, B.; Cheng, G.; Na, G. Occurrence and distribution of antibiotics and antibiotic resistance genes from the land to ocean in Daliao River-Liaodong Bay, China. *Mar. Environ. Res.* **2024**, *197*, 106470. [CrossRef]
2. Si, R.; Liu, X.; Pan, S.; Lu, Q.; Liu, M. Assessing the inhibitory effect and intervention mechanism of food traceability system on reducing hog farmers' overuse of animal antibiotics in China. *Food Policy* **2024**, *124*, 102619. [CrossRef]
3. Nkoh, J.N.; Shang, C.; Okeke, E.S.; Ejeromedoghene, O.; Oderinde, O.; Etafo, N.O.; Mgbechidinma, C.L.; Bakare, O.C.; Meugang, E.F. Antibiotics soil-solution chemistry: A review of environmental behavior and uptake and transformation by plants. *J. Environ. Manag.* **2024**, *354*, 120312. [CrossRef]
4. Huang, X.; Wen, D.; Wang, J. Radiation-induced degradation of sulfonamide and quinolone antibiotics: A brief review. *Radiat. Phys. Chem.* **2024**, *215*, 111373. [CrossRef]
5. Amangelsin, Y.; Semenova, Y.; Dadar, M.; Aljofan, M.; Bjorklund, G. The impact of tetracycline pollution on the aquatic environment and removal strategies. *Antibiotics* **2023**, *12*, 440. [CrossRef]
6. Hamid, I.; Khanday, W.A. Recent advances in antibiotic removal methods from wastewater: A comprehensive review. *Sep. Purif. Technol.* **2026**, *381*, 135478. [CrossRef]
7. Lin, Z.; Chen, Y.; Li, G.; Wei, T.; Li, H.; Huang, F.; Wu, W.; Zhang, W.; Ren, L.; Liang, Y.; et al. Change of tetracycline speciation and its impacts on tetracycline removal efficiency in vermicomposting with epigeic and endogeic earthworms. *Sci. Total Environ.* **2023**, *881*, 163410. [CrossRef]
8. Long, S.; Hamilton, P.B.; Wang, C.; Li, C.; Xue, X.; Zhao, Z.; Wu, P.; Gu, E.; Uddin, M.M.; Li, B.; et al. Bioadsorption, bioaccumulation and biodegradation of antibiotics by algae and their association with algal physiological state and antibiotic physicochemical properties. *J. Hazard. Mater.* **2024**, *468*, 133787. [CrossRef]
9. Xu, B.; Liu, F.; Brookes, P.C.; Xu, J. Microplastics play a minor role in tetracycline sorption in the presence of dissolved organic matter. *Environ. Pollut.* **2018**, *240*, 87–94. [CrossRef]
10. Chen, Y.; Li, J.; Wang, F.; Yang, H.; Liu, L. Adsorption of tetracyclines onto polyethylene microplastics: A combined study of experiment and molecular dynamics simulation. *Chemosphere* **2021**, *265*, 129133. [CrossRef]
11. Wang, F.; Wang, Z.; Zhao, Y.; Zhang, J. Performance of traditional and emerging water-treatment technologies in the removal of tetracycline antibiotics. *Catalysts* **2024**, *14*, 269. [CrossRef]
12. Li, Z.; Yang, W.; Xie, L.; Li, Y.; Liu, Y.; Sun, Y.; Bu, Y.; Mi, X.; Zhan, S.; Hu, W. Prominent role of oxygen vacancy for superoxide radical and hydroxyl radical formation to promote electro-Fenton-like reaction by W-doped CeO_2 composites. *Appl. Surf. Sci.* **2021**, *549*, 149262. [CrossRef]
13. Wang, J.; Zhuan, R.; Chu, L. The occurrence, distribution and degradation of antibiotics by ionizing radiation: An overview. *Sci. Total Environ.* **2019**, *646*, 1385–1397. [CrossRef]
14. Si, X.; Jin, Y.; Meng, X.; Huang, J. Electro-Fenton process for the treatment of antibiotics in water: A review. *ACS ES&T Water* **2026**, *6*, 4699–4717. [CrossRef]
15. Brillas, E. Electro-Fenton treatment of antibiotics in aqueous matrices. A review of recent development in the period 2022–2025. *Chemosphere* **2026**, *408*, 144986. [CrossRef]
16. Wang, Q.; Wang, L.; Wang, J.; He, X.; Wang, S.; Yan, A.; Zhang, Z.; Li, G.; Li, Y. Methods and prospects for enhancing heterogeneous Fenton catalytic activity. *Chem. Sel.* **2025**, *10*, e202404183. [CrossRef]
17. Udourioh, G.A.; Alikali, I.I.; Solomon, M.M.; Matthews-Amune, C.O. Environmental remediation using metal-organic frameworks: Recent progress in adsorption capacities, mechanisms, and practical applications. *J. Mol. Struct.* **2026**, *1351*, 144167. [CrossRef]

18. Wang, Z.; Wang, G.; Qi, H.; Wang, M.; Wang, M.; Park, S.; Wang, H.; Yu, M.; Kaiser, U.; Fery, A.; et al. Ultrathin two-dimensional conjugated metal–organic framework single-crystalline nanosheets enabled by surfactant-assisted synthesis. *Chem. Sci.* **2020**, *11*, 7665–7671. [CrossRef]
19. Yao, Y.; Han, Y.; Qi, S.; Sun, D.; Lang, J.; Hu, B.; Ma, Y.; Liu, C. Metal-free thiophene-based covalent organic frameworks achieve efficient photocatalytic hydrogen evolution by accelerating interfacial charge transfer. *Int. J. Hydrogen Energy* **2024**, *63*, 184–192. [CrossRef]
20. Zhang, H.; Zhou, Z.; Sun, X.; Zhang, Y.; Gao, Y. Metal organic framework MOF-74 based solid-state electrolytes for all-solid-state sodium metal batteries. *J. Solid State Chem.* **2024**, *334*, 124643. [CrossRef]
21. Li, Y.; Guo, Q.; Ding, Z.; Jiang, H.; Yang, H.; Du, W.; Zheng, Y.; Huo, K.; Shaw, L.L. MOFs-based materials for solid-state hydrogen storage: Strategies and perspectives. *Chem. Eng. J.* **2024**, *485*, 149665. [CrossRef]
22. Gayathri, K.; Vinothkumar, K.; Mohan, S.; Balakrishna, R.G. Manifestation of UiO-66-Zr MOF-enabled photocatalytic membranes for successive separation and degradation of dye mixtures in water remediation. *J. Environ. Chem. Eng.* **2024**, *12*, 112490. [CrossRef]
23. Guo, S.; Li, J.; Wang, Y.; Sun, D.; Ma, H.; Hao, J.; Wang, G.; Zhang, X. Polydopamine-modified bimetallic metal organic frameworks (MOFs) for peroxymonosulfate activation to efficient degradation of tetracycline hydrochloride in wastewater. *Colloids Surf. A Physicochem. Eng. Asp.* **2024**, *689*, 133721. [CrossRef]
24. Panda, S.; Kundu, S.; Malik, P.; Haldar, R. Leveraging metal node-linker self-assembly to access functional anisotropy of zirconium-based MOF-on-MOF epitaxial heterostructure thin films. *Chem. Sci.* **2024**, *15*, 2586–2592. [CrossRef]
25. Hou, S.; Chen, Z.; Luo, X.; Zhang, M.; Yang, P. Hydrogel immobilized bacteria@MOFs composite towards Bisphenol A degradation and the interconnection mechanism elucidation. *Environ. Res.* **2024**, *251*, 118718. [CrossRef]
26. Zhang, Z.; Chen, Y.; Wang, Z.; Hu, C.; Ma, D.; Chen, W.; Ao, T. Effective and structure-controlled adsorption of tetracycline hydrochloride from aqueous solution by using Fe-based metal-organic frameworks. *Appl. Surf. Sci.* **2021**, *542*, 148662. [CrossRef]
27. Jian, Y.; Zou, J.; Zheng, J.; Liao, D.; Lan, Q.; Prakash, O.; Liu, J.; Kumar, A.; Ouyang, J.; Pan, Y. Current status and prospect of MOF-74-based materials for biomedical applications. *J. Drug Deliv. Sci. Technol.* **2024**, *94*, 105470. [CrossRef]
28. Khan, W.A.; Arain, M.B.; Balal, S.; Mollahosseini, A.; Soylak, M. Deep eutectic solvent-functionalized metal-organic frameworks in sportive extraction techniques and their applications—A review. *Microchem. J.* **2025**, *212*, 113201. [CrossRef]
29. Yang, W.; Han, Y.; Li, C.; Zhu, L.; Shi, L.; Tang, W.; Wang, J.; Yue, T.; Li, Z. Shapeable three-dimensional CMC aerogels decorated with Ni/Co-MOF for rapid and highly efficient tetracycline hydrochloride removal. *Chem. Eng. J.* **2019**, *375*, 122076. [CrossRef]
30. Niu, Y.; Jiang, P.; Guo, T. A MOFs/MIPs@GAs ternary composite catalytic system with graphene oxide aerogels as the multifunctional skeleton for high-efficiency detoxification of organophosphate nerve agents in pure water. *ACS Appl. Mater. Interfaces* **2024**, *16*, 49305–49317. [CrossRef]
31. Fu, J.-X.; Li, S.-Y.; Li, Q.-Y.; Bell, E.; Yang, D.-D.; Li, T.; Li, Y.-J.; He, J.-Y.; Zhou, L.-D.; Zhang, Q.-H.; et al. Preparation of surface molecular-imprinted MOFs for selective degradation of tetracycline antibiotics in wastewater. *Colloids Surf. A Physicochem. Eng. Asp.* **2024**, *687*, 133575. [CrossRef]
32. Roozbeh, R.; Keramati, N.; Mousavi Kamazani, M. Enhanced removal of tetracycline using amine-modified ZIF-11: Isotherms, kinetics, and thermodynamics. *Sci. Rep.* **2026**, *16*, 22673. [CrossRef]
33. Liang, Y.; Liu, C.; He, X.; Zhou, L.; Ju, N. Removal of tetracycline from wastewater using magnetic metal–organic frameworks: Performance and mechanism. *Appl. Organomet. Chem.* **2026**, *40*, e70599. [CrossRef]
34. Feng, Q.; Zhou, Y.; Shi, L.; Wang, K.; Jiao, Q.; Zhang, Q.; Chen, W.; Liu, J. Room-temperature synthesis of Ce/Fe-based metal–organic framework for efficient Fenton-like photocatalytic degradation of tetracycline in water. *Cryst. Growth Des.* **2026**, *26*, 5713–5724. [CrossRef]
35. Sun, C.; Yu, Y.; Lu, Y.; Wang, F.; Liu, J.; Zhai, W.; Gao, X. Fe-driven specificity and Z-scheme catalysis in MOF nanocomposites for targeted discrimination and degradation of tetracycline antibiotics. *ACS Appl. Nano Mater.* **2026**, *9*, 3740–3751. [CrossRef]
36. Gangola, S.; Joshi, S.; Kumar, A.; Garg, S.; Bhandari, N.S.; Lekhwar, R.; Gaurav, K.; Saraswat, A.; Thanka, P.P.; Kumar, S.; et al. Exopolysaccharides: Promising applications in bioremediation for waste removal. *Front. Microbiol.* **2026**, *17*, 1859365. [CrossRef]
37. De Bruin, S.; Riisgaard-Jensen, M.; Hansen, S.H.; Van Loosdrecht, M.C.M.; Nielsen, P.H.; Lin, Y. Global insights into extracellular polymeric substances from activated sludge: Yield, composition, and microbial communities. *Water Res.* **2026**, *289*, 124726. [CrossRef]
38. Du, Y.; Zhao, S.; Gao, Y.; Yan, Y.; Kong, Y.; Meng, W.; Lu, X.; Zheng, S.; Mu, H.; Chen, X.; et al. The synergistic effect of algal-bacterial granular sludge in a sequencing batch reactor with tetracycline-containing synthetic livestock and poultry breeding wastewater. *J. Environ. Manag.* **2026**, *402*, 129178. [CrossRef]
39. Chen, X.; Liu, X.; Zhu, L.; Tao, X.; Wang, X. One-step fabrication of novel MIL-53(Fe, Al) for synergistic adsorption-photocatalytic degradation of tetracycline. *Chemosphere* **2022**, *291*, 133032. [CrossRef]

40. Barbosa, A.D.S.; Julião, D.; Fernandes, D.M.; Peixoto, A.F.; Freire, C.; de Castro, B.; Granadeiro, C.M.; Balula, S.S.; Cunha-Silva, L. Catalytic performance and electrochemical behaviour of metal–organic frameworks: MIL-101(Fe) versus NH_2-MIL-101(Fe). *Polyhedron* **2017**, *127*, 464–470. [CrossRef]
41. Singh, N.; Dalakoti, S.; Sharma, A.; Chauhan, R.; Murali, R.S.; Divekar, S.; Dasgupta, S.; Aarti. Shaping of MIL-53-Al and MIL-101 MOF for CO_2/CH_4, CO_2/N_2 and CH_4/N_2 separation. *Sep. Purif. Technol.* **2024**, *341*, 126820. [CrossRef]
42. Nguyen, K.G.; Nguyen, D.T.C. Synthesis, functionalization, adsorption performance and mechanism of MIL-53(Fe)-based materials for wastewater treatment. *J. Ind. Eng. Chem.* **2026**, *161*, 169–191. [CrossRef]
43. Pei, S.; You, S.; Ma, J.; Chen, X.; Ren, N. Electron spin resonance evidence for electro-generated hydroxyl radicals. *Environ. Sci. Technol.* **2020**, *54*, 13333–13343. [CrossRef]
44. Shoji, T.; Li, L.; Abe, Y.; Ogata, M.; Ishimoto, Y.; Gonda, R.; Mashino, T.; Mochizuki, M.; Uemoto, M.; Miyata, N. DMPO-OH radical formation from 5,5-dimethyl-1-pyrroline N-oxide (DMPO) in hot water. *Anal. Sci.* **2007**, *23*, 219–221. [CrossRef]
45. Wierzbicki, S.; Douglin, J.C.; Singh, R.K.; Dekel, D.R.; Kruczała, K. Operando EPR study of radical formation in anion-exchange membrane fuel cells. *ACS Catal.* **2023**, *13*, 2744–2750. [CrossRef]
46. Cui, K.P.; He, Y.Y.; Xu, K.J.; Zhang, Y.; Chen, C.B.; Xu, Z.J.; Chen, X. Degradation of tetracycline hydrochloride by Cu-doped MIL-101(Fe) loaded diatomite heterogeneous Fenton catalyst. *Nanomaterials* **2022**, *12*, 811. [CrossRef]
47. Luo, Y.; Su, R. Preparation of NH_2-MIL-101(Fe) metal organic framework and its performance in adsorbing and removing tetracycline. *Int. J. Mol. Sci.* **2024**, *25*, 9855. [CrossRef]
48. Wang, F.-X.; Zhang, Z.-C.; Wang, C.-C. Selective oxidation of aqueous organic pollutants over MOFs-based catalysts: A mini review. *Chem. Eng. J.* **2023**, *459*, 141538. [CrossRef]
49. Duan, S.; Lin, Y.; Lan, G.; Jing, Y.; Talha, M. Optimization and mechanism exploration of NH_2-functionalized MIL-101(Fe) for enhanced adsorption of antibiotics in single and binary systems: Experimental analysis and DFT calculations. *J. Environ. Chem. Eng.* **2025**, *13*, 119456. [CrossRef]
50. Hamid, U.; Chen, C.-C. Adsorption thermodynamics for process simulation. *Langmuir* **2024**, *40*, 23583–23597. [CrossRef]
51. Vigdorowitsch, M.; Pchelintsev, A.; Tsygankova, L.; Tanygina, E. Freundlich isotherm: An adsorption model complete framework. *Appl. Sci.* **2021**, *11*, 8078. [CrossRef]
52. Ezzati, R.; Azizi, M.; Ezzati, S. A theoretical approach for evaluating the contributions of pseudo-first-order and pseudo-second-order kinetics models in the Langmuir rate equation. *Vacuum* **2024**, *222*, 113018. [CrossRef]
53. Yue, J.; Zheng, Q.; Ding, S.; Yin, Y.; Zhang, X.; Wang, L.; Gu, Y.; Li, J.; Zhang, Y.; Shi, Y.; et al. Cu-Co bimetallic organic framework as effective adsorbents for enhanced adsorptive removal of tetracycline antibiotics. *Sci. Rep.* **2024**, *14*, 17607. [CrossRef]
54. El Aamri, M.; Khalki, Y.; Mohammadi, H.; Amine, A. Development of an innovative colorimetric DNA biosensor based on sugar measurement. *Biosensors* **2023**, *13*, 853. [CrossRef]
55. Bashirova, N.; Butenschön, E.; Poppitz, D.; Gaß, H.; Halik, M.; Dentel, D.; Tegenkamp, C.; Matysik, J.; Alia, A. Magnetic resonance imaging-based monitoring of the accumulation of polyethylene terephthalate nanoplastics. *Molecules* **2024**, *29*, 4380. [CrossRef]
56. Guan, L.; Zhou, Y.; Yang, S. An improved prediction model for COD measurements using UV-Vis spectroscopy. *RSC Adv.* **2024**, *14*, 193–205. [CrossRef]

Disclaimer/Publisher's Note: The statements, opinions and data contained in all publications are solely those of the individual author(s) and contributor(s) and not of MDPI and/or the editor(s). MDPI and/or the editor(s) disclaim responsibility for any injury to people or property resulting from any ideas, methods, instructions or products referred to in the content.